BRNO UNIVERSITY OF TECHNOLOGY
VYSOKÉ UČENÍ TECHNICKÉ V BRNĚ

FACULTY OF MECHANICAL ENGINEERING
FAKULTA STROJNÍHO INŽENÝRSTVÍ

INSTITUTE OF PHYSICAL ENGINEERING
ÚSTAV FYZIKÁLNÍHO INŽENÝRSTVÍ

IMAGING OF AN OBJECT IN TURBID MEDIUM BY COMBINING THE SIGNAL OF BALLISTIC AND DIFFUSE PHOTONS IN THE COHERENCE-CONTROLLED HOLOGRAPHIC MICROSCOPE

ZOBRAZENÍ OBJEKTU V ROZPTYLUJÍCÍM PROSTŘEDÍ KOMBINACÍ SIGNÁLU BALISTICKÝCH A ROZPTÝLENÝCH FOTONŮ V KOHERENCÍ ŘÍZENÉM HOLOGRAFICKÉM MIKROSKOPU

MASTER'S THESIS
DIPLOMOVÁ PRÁCE

AUTHOR — **Bc. Miroslav Ďuriš**
AUTOR PRÁCE

SUPERVISOR — **prof. RNDr. Radim Chmelík, Ph.D.**
VEDOUCÍ PRÁCE

BRNO 2018

BRNO UNIVERSITY OF TECHNOLOGY
FACULTY OF MECHANICAL ENGINEERING

Master's Thesis Assignment

Institut:	Institute of Physical Engineering
Student:	**Bc. Miroslav Ďuriš**
Degree programm:	Applied Sciences in Engineering
Branch:	Precise Mechanics and Optics
Supervisor:	**prof. RNDr. Radim Chmelík, Ph.D.**
Academic year:	2017/18

As provided for by the Act No. 111/98 Coll. on higher education institutions and the BUT Study and Examination Regulations, the director of the Institute hereby assigns the following topic of Master's Thesis:

Imaging of an object in turbid medium by combining the signal of ballistic and diffuse photons in the coherence-controlled holographic microscope

Brief description:

The special feature of coherence-controlled holographic microscope is its capability to image samples in optically turbid media using the signal of not only ballistic and snake photons, but also photons strongly (multiply) scattered by the turbid medium. The imaging mode is selected by adjusting the microscope optical system. Combining images of the same sample in different modes improves the quality of resulting image and its signal-to-noise ratio. The principle of this advanced imaging method is experimentally verified on a model sample. It is necessary to design and experimentally verify the procedure for its routine use.

Master's Thesis goals:

1. Design a method for routine observation of objects in optically turbid medium using the combination of the signals of ballistic and heavily scattered photons.
2. Design and prepare a suitable model sample, and verify the method experimentally.

Recommended bibliography:

BORN, M., Wolf, E., Principles of Optics, 7th Exp.Ed. Cambridge Univ. Press, Cambridge 2002.

SLABÝ, T., KOLMAN, P., DOSTÁL, Z., ANTOŠ, M., LOŠŤÁK, M., CHMELÍK, R., Off-axis setup taking full advantage of incoherent illumination in coherence-controlled holographic microscope, OPTICS EXPRESS, Vol. 21, No. 12 (2013), pp. 14747-14762.

CHMELÍK, R., SLABÁ, M., KOLLÁROVÁ, V., SLABÝ, T., LOŠŤÁK, M., ČOLLÁKOVÁ, J., DOSTÁL, Z., The Role of Coherence in Image Formation in Holographic Microscopy, PROGRESS IN OPTICS, Vol. 59 (2014), pp. 267-335.

LOŠŤÁK, M., CHMELÍK, R., SLABÁ, M., SLABÝ, T., Coherence-controlled holographic microscopy in diffuse media, OPTICS EXPRESS, Vol. 22, No. 4 (2014), pp. 4180-4195.

KOLLÁROVÁ, V., ČOLLÁKOVÁ, J., DOSTÁL, Z., VESELÝ, P., CHMELÍK, R., Quantitative phase imaging through scattering media by means of coherence-controlled holographic microscope, JOURNAL OF BIOMEDICAL OPTICS, Vol. 20, No. 11 (2015), 111206.

Students are required to submit the thesis within the deadlines stated in the schedule of the academic year 2017/18.

In Brno, 7. 11. 2017

VYSOKÉ UČENÍ TECHNICKÉ V BRNĚ FAKULTA STROJNÍHO INŽENÝRSTVÍ

L. S.

prof. RNDr. Tomáš Šikola, CSc.
Director of the Institute

doc. Ing. Jaroslav Katolický, Ph.D.
FME dean

Summary
This thesis deals with the quantitative phase imaging (QPI) of objects behind scattering media in coherence-controlled holographic microscope (CCHM). It is possible to image in this microscope with completely incoherent illumination, which gives rise to the coherence-gating effect. It is a crucial property that allows the separation of ballistic and multiply scattered photons, therefore, a part of the thesis explains in depth the coherence-gate. Fundamentals of the image formation in CCHM are presented, which support many interpretations of results throughout the experimental part of the work.

The goal of the thesis is to design a method for an observation of phase objects in turbid milieu and experimentally prove the method working. A novel method based on the preliminary research and the analytical derivation is proposed. It is based on an acquisition of multiple images for different reference field shifts. Each shift corresponds to the imaging by a different group of photons. The particular QPIs formed by ballistic or scattered photons can be superposed to create synthetic image of improved quality. Experiments with variously complex samples provided information about limitations of this method.

Abstrakt
Diplomová práca sa zaoberá kvantitatívnym fázovým zobrazovaním objektov umiestnených za rozptyľujúcim prostredím v koherenciou riadenom holografickom mikroskope. Tento mikroskop umožnuje zobrazovať s úplne nekoherentným osvetlením vzorky, čo vyvoláva efekt koherenčnej brány. Koherenčná brána je veľmi dôležitá vlastnosť zobrazovacieho systému umožňujúca separáciu balistických a rozptýlených fotónov, jej dôkladnému vysvetleniu je venovaná značná časť práce. Ďalej sú prezentované základy teórie zobrazenia v koherenciou riadenom holografickom mikroskope. Tie sú využité v závere práce pri interpretácii experimentálnych výsledkov.

Cieľom práce je navrhnúť metódu pre pozorovanie fázových objektov v rozptyľujúcich prostrediach a experimentálne túto metódu overiť. Na základe analytických výsledkov a predchádzajúceho výskumu je navrhnutá nová metóda, ktorá je ďalej overovaná pomocou rôzne komplexných vzoriek. Je založená na zázname viacerých obrazov s rôznym posunutím referenčného poľa. Každý posun korešponduje so zobrazovaním pomocou inej skupiny fotónov. Je možné vytvoriť syntetický obraz so zlepšenou kvalitou sčítaním jednotlivých obrazov získaných z interferencie balistických alebo rozptýlených fotónov. Experimenty s rôzne komplexnými vzorkami poskytujú náhľad na obmedzenia prezentovanej metódy.

Keywords
holographic microscopy, imaging in turbid media, coherence gate

Kľúčové slová
holografická mikroskopia, zobrazovanie v opticky kalných prostrediach, koherenčná brána

ĎURIŠ, M. *Imaging of an object in turbid medium by combining the signal of ballistic and diffuse photons in the coherence-controlled holographic microscope.* Brno: Brno University of Technology, Faculty of Mechanical Engineering, 2018. 56 p. Supervisor prof. RNDr. Radim Chmelík, Ph.D.

I declare that I have written this thesis on my own with the help of expert supervision provided by prof. RNDr. Radim Chmelík, Ph.D. and using the sources listed in the bibliography at the end of this thesis.

May 25, 2018 Bc. Miroslav Ďuriš

I would like to express thanks to my master's thesis supervisor prof. RNDr. Radim Chmelík, Ph.D., for his expert guidance and discussions as well as valuable suggestions on improving my thesis. I would like to thank also to Ing. Lenka Štrbková, Ph.D. for tremendous help with experimental work. A special thanks to my family for the excellent care and support I was provided by during my whole studies.

Bc. Miroslav Ďuriš

Contents

1. Introduction

An imaging of biological and medical samples by means of light has been for a long time confined to the observation of the sample surface and phenomena happening in its immediate vicinity. Over the last few decades, an extensive research, to overcome this limitation and to non-invasively image objects inside turbid media, has been carried out. The rapid progress in the field has been propelled by the development of the laser, data acquisition systems, imaging technologies and corresponding experimental tools. Developed techniques exploit the fact that many biomedical objects are weakly absorbing in comparison to the strength of the light scattering [1]. The object information is not destroyed by the scattering process, therefore, it is possible to retrieve an object image out of the scattered light.

The first emerging imaging techniques were based on the separation of the least scattered (ballistic or first-arriving) light, which is believed to carry the most reliable image information about a specimen, from the diffuse (multiply scattered) component. Various principles of the ballistic light separation are established, such as spatial filtering, polarization gating, time gating and coherence gating. The simplest system is a confocal microscope [2–4]. A point in the focus is imaged through a pinhole onto the detector. The pinhole provides the spatial filtering to exclude the diffuse light component. It works effectively until the ballistic signal becomes smaller than the background and noise. The polarization gating relies on the fact that multiply scattered light loses its former polarization state, and therefore, can be partially suppressed by a polarizer. Time gating techniques are made possible by the development of electro-optical components, which allow ultrashort pulse generation and correspondingly fast data acquisition. The first-arriving light is either gated, for example by optical Kerr gate [5], or separated in the post processing of the data, acquired by streak camera [6]. Holographic methods exploit properties of a source, providing an illumination of the examined specimen, to coherence gate the ballistic light [7–12]. Imaging in a spatially and temporally low coherent light is analogous to the spatial filtering of a confocal microscope and the time gating, respectively [9, 12].

Practical implementations of techniques that use also the diffuse component of the scattered light, is made possible by the increased computational power of computers over the recent years. Among these methods belong for example diffuse optical tomography [13], which exploits the diffusion approximation [14] to computationally reconstruct an object, digital phase conjugation and wavefront optimization [15, 16], methods involving image reconstruction of the object based on the a priori knowledge of the transmission matrix of the scattering medium [17, 18], a deconvolution technique [19], which uses measured point spread function (PSF) of the diffuser, where the PSF is valid only in a limited angular memory-effect range [20].

This thesis deals with the use of the holographic microscope and its coherence gating properties in the imaging through scattering media. Coherence-controled holographic microscope (CCHM) is a microscopic system, based on Leith's and Upatnieks' concept of incoherent holography [21], developed by the Experimental Biophotonics group. Its latest version, designed by Tomas Slaby [11], was used to carry out experiments, which are presented later in the thesis. Digital holography techniques provide one major advantage over most of the previously mentioned methods of imaging through turbid media. That is, they provide a quantitative phase image (QPI) of translucent objects. QPI in turbid media, with the use of CCHM, of both model objects [22] and live cells [23] has been demonstrated experimentally. The theory and experiments [12, 24] suggest that CCHM is capable of QPI through a scattering medium using not only ballistic light, but also multiply scattered light, which is in other methods usually suppressed and never used for a direct image formation.

The first goal of the research presented in this thesis is to devise a method for a routine observation of a specimen in a turbid milieu using ballistic and strongly scattered photons. The preliminary research suggests that a combination of ballistic and multiply scattered photons may improve the quality of QPI, therefore, a part of the thesis deals with a generation of synthetic images by combining the ballistic and scattered photons. The second goal is to design a model sample, which can be used to confirm the proposed method experimentally.

In Chap. 2 is presented a brief introduction to the scattering by biological tissues. Chap. 3 deals with the image formation theory of CCHM and methods of image synthesis. The synthesis process and its fundamentals are then evaluated by experiments presented in Chap. 4.

2. Scattering by tissue and random media

2.1 Physical basics of scattering and absorption

Scattering of an electromagnetic wave is caused by the heterogeneity of a system the wave is interacting with. Regardless of the type and scale of the heterogeneity, the physics behind the scattering is the same in all cases. If an obstacle, composed of discrete electric charges, is illuminated by an electromagnetic wave, electric charges in the obstacle are being accelerated and set into oscillatory motion by the electric field of the incident wave. An electromagnetic radiation of the oscillating charges is called secondary radiation, and forms the scattered electromagnetic field. Absorption is

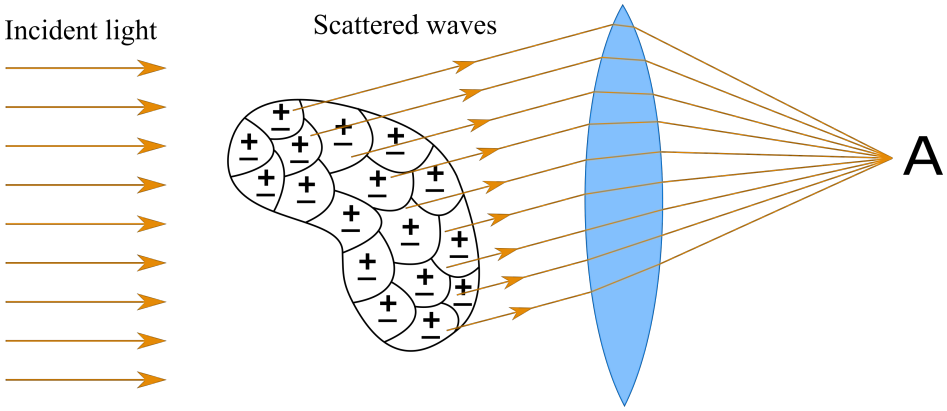

Figure 2.1: Scattered radiation by a particle formed by electric dipoles. Figure is based on the illustrations in [25].

a process that transforms part of the incident electromagnetic energy into other forms, for example thermal energy. Scattering and absorption are not mutually independent, and therefore, often by referring to scattering, also absorption is meant to take place. A qualitative understanding of scattering can be acquired by assuming a single particle dividable into small subregions (see Fig. 2.1). An electromagnetic oscillating field applied on the particle induces a dipole moment in each region. Oscillation of these dipoles at the field frequency scatter secondary radiation in all directions. Coherent superposition of the scattered waves provides an information about the total field in a particular direction (distant point A). Phase differences has to be taken into account, because in general phase relations between the waves are different for each scattering direction. If the particle is small compared to the wavelength of the light, phase differences of waves originating from different dipoles are negligible. Therefore, very low variation of scattering with direction is expected. However, as the particle size increases also possibilities for constructive and destructive interference of the scattered waves

increase. Thus, more peaks and valleys in the scattering pattern appear. The shape of scattered fields depends on many characteristics of the particle or the heterogeneity in general, such as size, shape or material properties. The elastic scattering can be divided into three regimes (Geometric scattering, Mie scattering, Rayleigh scattering) based on the size parameter ($2\pi a/\lambda$), where a is the radius of a spherical particle, λ is the wavelength of the incident light. The scattering regime depends on the particle size, the electromagnetic radiation wavelength and optical properties relative to the surrounding medium (i.e. the complex refractive index), as shown in Fig. 2.2 [25].

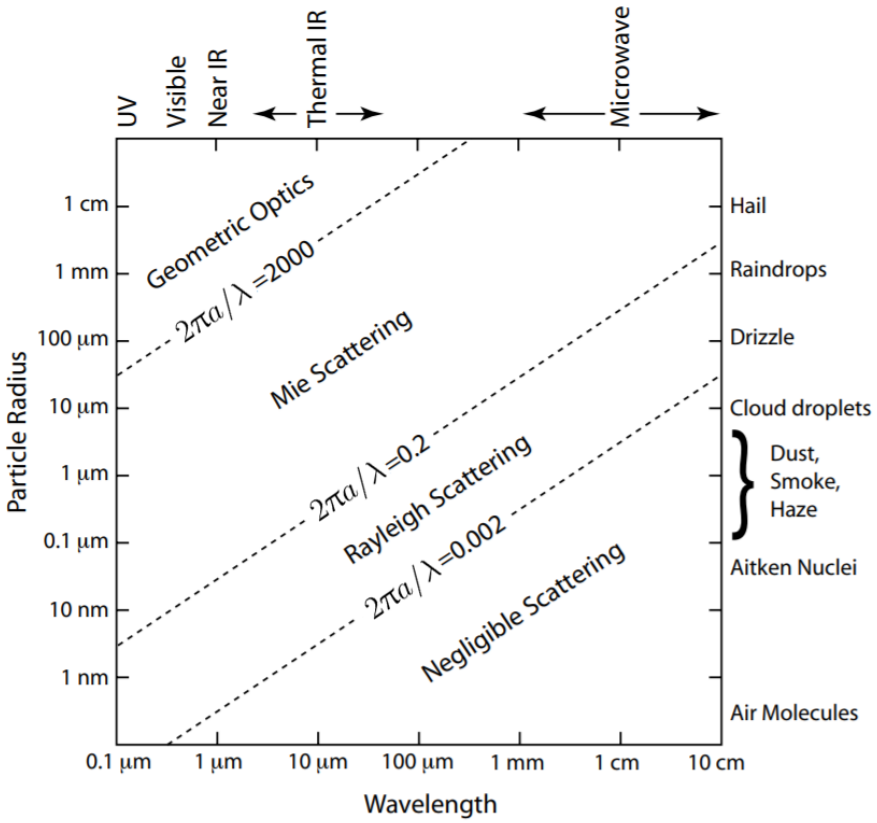

Figure 2.2: Regimes of the elastic scattering divided based on the size parameter ($2\pi a/\lambda$), the is figure adapted from [26].

2.2 Biological tissue structure

Biological tissues are optically inhomogeneous, interconnected and arbitrarily shaped structures. Light propagation within a tissue depends on the scattering and absorption properties of cells, cell organelles, various fiber structures and surrounding milieu. Important roles in the propagation of light in tissues play the size, shape and optical density of aforementioned structures and also polarization state of the incident wave. In the illustrative figure 2.3 a part of a skin tissue is shown to be composed of many different biological components. Membranes, muscle and connective tissue fibers, cells, cell organelles and vessels are all of different shapes and optical properties. They represent heterogeneities of refractive index, which induce the light scattering.

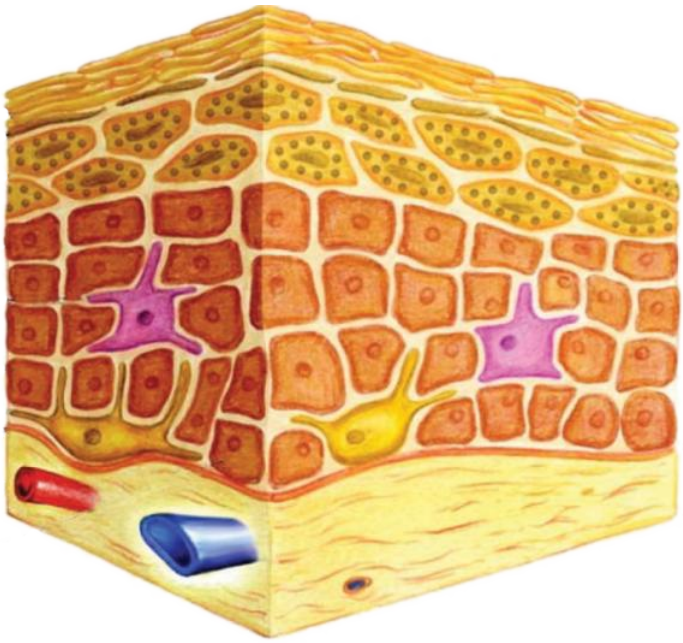

Figure 2.3: Three dimensional illustration of a skin fragment showing various structural components of the biological tissue, adapted from [27].

With regards to the diversity and structural complexity of tissues, it can be concluded, that the greatest challenge in tissue studies is a development of an adequate optical model accounting for the scattering and absorption of electromagnetic radiation. There are two most common approaches used for tissue modeling. One of them assumes a tissue to be a medium with a continuous random spatial distribution of optical properties, the other approach models tissue as an ensemble of discrete scatterers. Whether the first or second approach is chosen depends on the examined tissue structure and its scattering characteristics [28–34]. Tissues without pronounced boundaries between elements can be adequately modeled as a random continuum of inhomogeneities with various spatial size. The process of scattering in these structures may be described by using the model of a phase screen [35]. In this theory, it is assumed that the random medium can be strong enough to cause a significant deformation of the wavefront, but the screen is so thin, that only the phase modulation occurs. The second approach to tissue modeling uses a representation with a system of discrete scattering particles. It is suitable for biological media because they are comprised of cells that are similar to spheres or ellipsoids in shape. The scattering of light on spherical particles is rigorously described by the Mie theory [25]. Solution for diffraction on a long cylinder is also well understood, which helps to model scattering by fiber structures [25].

Tissue structure components vary over a wide range of scales. Cells themselves take on various shapes and sizes (order of tens of micrometers) in different parts of tissue. A cell contains other smaller structures such as membranes (with a thickness about 10 nm) and organelles including the nucleus (with a size from 5 µm to 10 µm), mitochondria (with characteristic dimensions ranging from 0.2 µm to 2 µm), and many other structures as shown in Fig. 2.4. In fibrous tissue, a typical diameter of the cylindrical structures is from 10 nm to 400 nm and their length ranges from 10 µm to

a few millimeters [28, 29].

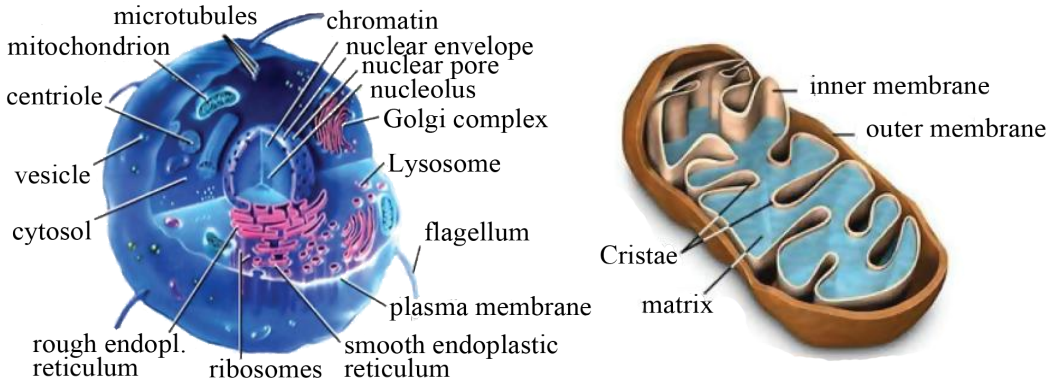

Figure 2.4: Major organelles and inclusions of the cell and the mitochondrion structure, figures reproduced from [28].

2.3 Rayleigh scattering

Small particles with respect to the wavelength of the incident light scatter as if they were single dipoles. The Rayleigh theory describes this case if condition $m(2\pi a/\lambda) \ll 1$ is satisfied. The quantity $m = n_{\mathrm{S}}/n_{\mathrm{medium}}$ is relative refractive index of the scatterers, n_{S} and n_{medium} are refractive indices of scatterer and medium, respectively, a is the radius of the particle and λ is the wavelength of the incident light. Using this theory, angular distribution of the scattered unpolarized light of intensity I_0 by an ensemble of N randomly distributed particles can be calculated at the distant detector position. Mean distance between particles must be bigger than the wavelength λ, so the following formula according to [25, 36, 37] holds

$$I(r,\theta) = (2\pi)^4 \frac{a^6}{\lambda^4 r^2} \left(\frac{m^2 - 1}{m^2 + 2} \right)^2 N \frac{1 + \cos^2 \theta}{2} I_0, \tag{2.1}$$

where r is the distance of the detector and θ is the scattering angle. Assuming near-infrared light and biological scatterers with $m = 1.05 - 1.10$, the upper limit of the radius a, when the Rayleigh theory is still valid, is about $12-14\,\mathrm{nm}$. The problem of the scattering by a special class of arbitrarily shaped particles is addressed by the Rayleigh-Gans-Debye theory [25,38]. It requires two conditions to be satisfied: $|m-1| \ll 1$ and $2\pi a'/\lambda |m-1| \ll 1$, where a' is the largest dimension of the particle. These conditions ensure that the electric field inside the particle is similar to the incident field and the particle can be viewed as a collection of independent dipoles exposed to the same field. The Rayleigh-Gans-Debye theory can be used to model larger particles, for example, when $m = 1.015$ and near-infrared light is used, validity is up to $a' = 950\,\mathrm{nm}$. It is, therefore, applicable for description of the light scattering on cell components (mitochondria, lysosomes, peroxisomes, etc) due to their small dimensions and refraction. Examples are adapted from [37].

2.4 Mie scattering

Mie scattering theory is based on an exact solution of Maxwell's equations for a homogeneous sphere [25, 36]. The theory deals with comparably large spherical particles with size of the order of the incident light wavelength. A similar formula to (2.1) can be derived to describe angular distribution of the scattered light intensity by an ensemble of N randomly distributed Mie particles, with the mean distance between them bigger than the wavelength λ, illuminated by an unpolarized electromagnetic wave of intensity I_0. The formula has the following form

$$I(\theta) = p^{\mathrm{Mie}}(\theta) N I_0, \tag{2.2}$$

where $p^{\mathrm{Mie}}(\theta)$ is the Mie phase function [37]. The derivation of the phase function is rather extensive and not needed for this thesis, therefore, it is skipped. As $p^{\mathrm{Mie}}(\theta)$ does not have a simple and straight-forward form, many approximations and empirical expressions are being used to model Mie scattering [39]. One of the most often exploited is the Henyey-Greenstein [40] phase function

$$p^{\mathrm{HG}}(\theta) = \frac{1}{4\pi} \cdot \frac{1 - g^2}{(1 + g^2 - 2g\cos\theta)^{3/2}}. \tag{2.3}$$

The Henyey-Greenstein phase function has one parameter g called the asymmetry factor. There are several ways to calculate the value of g, for more information see [37,39].

Despite the fact that Mie theory is strictly applicable only to particles of particular regular shapes, it can still provide useful results for modeling of actual biological tissues. Sometimes, a mixture of large particles contributing to high scattering anisotropy and small particles, which increase scattering of light with shorter wavelengths, can be a good approximative tissue model.

2.5 Scattering layer model

In previous studies of the image formation through scattering media [12, 22, 41], a scattering layer was modeled as an ensemble of diffraction gratings of various fringe frequencies. The scattering effect of a transmission diffraction grating, as shown in Fig. 2.5, illuminated by a monochromatic plane wave with the wavelength λ is a well-known phenomenon. It scatters a plane wave into several diffraction orders, each having a particular propagation angle θ_l. These angles can be calculated by the formula [36, Chap. 8]

$$\theta_l = \arcsin\left(\sin\theta_{\mathrm{i}} + \frac{l\lambda}{d}\right), \tag{2.4}$$

where θ_{i} is the angle of incidence, l is an integer representing the diffraction order and d is the grating period. Despite the fact that the derivation of the grating formula (2.4) is based on an idealized grating, the relation between angles of diffracted beams, the grating spacing and the wavelength of the light holds for any periodic structure of the

same spacing (period). The experimental study [42] of isolated frog semitendinosus

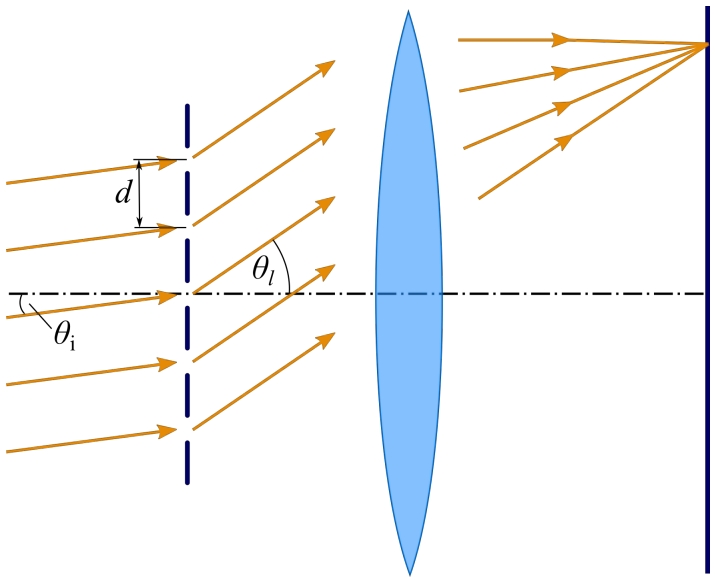

Figure 2.5: Schematic of the light diffraction of a transmission grating.

muscle fibers has shown that even biological tissue has structures that scatter light as a diffraction grating. Biological tissues often have a fibrous structure, which behaves as an ensemble of diffraction gratings with different spacing parameters, spatial orientations, shifts or transmission properties. Therefore, further in this work scattering medium is being modeled in calculations as structures similar to diffraction gratings.

3. Methods and imaging principles

3.1 Quantitative phase imaging

Translucent objects, like a living human cell, usually absorb and scatter just small amounts of light. This makes translucent objects difficult to observe in bright-field microscopes. Tissue structures induce phase shifts to the incident light wave, which can be visualized by several techniques. First solution to the imaging of light phase delays was proposed by Dutch physicist Frits Zernike in 1934 [43]. His phase contrast imaging using phase plate allows to observe cells in high contrast, but this technique does not provide quantitative information. This drawback is solved by interferometric methods like digital holography, which provide quantitative amplitude and phase-contrast imaging. Phase difference $\varphi_{\text{cell}}(x,y)$ induced by a cell with the homogeneous refractive

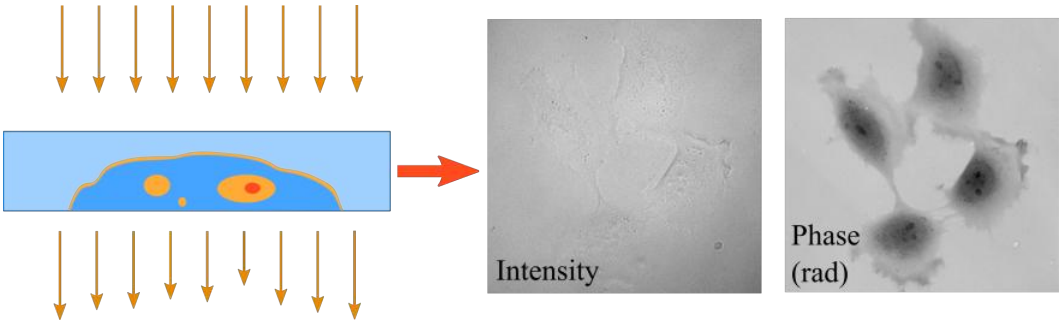

Figure 3.1: Quantitative phase imaging illustration. Phase retardation of the light passing the inner area of the cell, nucleus and other intracellular organelles gives rise to the contrast image of the specimen

index distribution n_{cell} surrounded by a medium of the refractive index n_{medium} can be described by the following relation

$$\varphi_{\text{cell}}(x,y) = \frac{2\pi}{\lambda} d_{\text{cell}}(x,y)(n_{\text{cell}} - n_{\text{medium}}), \tag{3.1}$$

where $d_{\text{cell}}(x,y)$ is cell thickness, λ is the light wavelength, and x,y are spatial coordinates in the object plane. For the further study of cells and tissues, it is convenient to have an information about cellular dry-mass density $\mu(x,y)$, which is proportional to the phase retardation induced by a cell

$$\mu(x,y) \approx \frac{1}{\alpha} \lambda \varphi(x,y). \tag{3.2}$$

Constant α is known as the specific refractive increment [44–46].

3.2 Microscope optical setup

Coherence-controlled holographic microscope (CCHM) has been designed by Tomas Slaby [11] to be used for a quantitative observation of phase samples (transparent but altering the phase of the light), such as cells or other biological samples, in transmission. Therefore, the setup is based on the Mach-Zehnder interferometer (see Fig. 3.2). The illumination beam emitted by an incoherent light source (LS) (a halogen-tungsten lamp coupled into an optical cable with aperture stop (A) and interference filter (IF) attached controlling the degree of spatial and temporal coherence, respectively) is split and propagates through two separated optical paths formed by identical microscope setups – condensers (C), infinity-corrected objectives (O) and tube lenses (TL). Reference (R) and specimen (S) planes are optically conjugated with the output plane (OP). Diffraction grating (DG) is an essential component of the CCHM. In this setup the

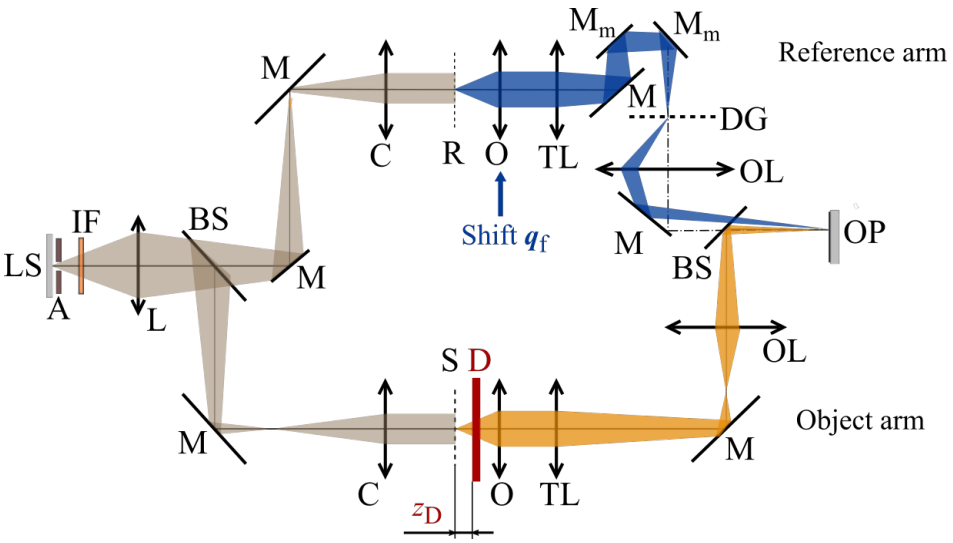

Figure 3.2: Optical set-up of coherence-controlled holographic microscope (CCHM). LS – light source, a – aperture stop of adjustable size, IF – interference filter, L – collector lens, BS – beam splitters, M – mirrors, Mm – movable mirrors, C – condenser lenses, R – reference plane, S – specimen (object) plane, D – diffuser, O – objective lenses, TL – tube lenses, OL – output lenses, DG – diffraction grating, OP – output plane.

transmission grating is placed in the reference arm and imaged onto the output plane (OP) according to the incoherent holography principle proposed by Leith and Upatnieks [21]. The use of the first diffraction order (other diffraction orders are eliminated by spatial filtering) for imaging results in spatially modulated reference beam by linear phase in the output plane. In the object arm, the diffraction grating is replaced by a mirror, which is equivalent to using the zeroth diffraction order. After recombination of the reference and the object beam in the output plane (OP) interference fringe pattern of the hologram[1] appears. The fringe frequency – i.e. the hologram carrier frequency f_C – is proportional to the spatial frequency f_G of diffraction grating grooves, unlike in the conventional off-axis holography microscope, where it is proportional to

[1] image containing information about the amplitude and the phase of the light in the image plane

the introduced reference beam tilt

$$f_{\mathrm{C}} = \frac{f_{\mathrm{G}}}{\mathrm{m_{OL}}}, \tag{3.3}$$

where $\mathrm{m_{OL}}$ is the magnification of output lens.

The Köhler illumination is provided by imaging the light source (LS) by collector lens (L) to the front focal planes of condensers (C). The use of the Köhler illumination in combination with aperture stop (A) allows to control the spatial coherence of the illumination, which is crucial in many experiments, including a few mentioned in Chap. 4. There are also some drawbacks of using highly incoherent illumination and one of them are high demands on precise alignment of optical components. Simple and fully automatable procedure was developed to align microscope easily. The first step is a translation of the reference arm objective perpendicularly to the optical axis to overlay the field-stop images formed by the reference and object arms in the output plane (OP). The translation is provided by a piezo-actuator. This movement is used not only for the alignment, but also for a novel imaging method proposed later in this work. Second step of the microscope set up procedure is an optical path equalization, which is carried out by shifting movable mirrors ($\mathrm{M_m}$) along the optical axis.

3.2.1 Complex image reconstruction of a hologram

A CCD camera chip placed in the output plane (OP) of the microscope captures fringe patterns formed by the interference of the object and the reference beam. The CCD camera is able to record only an intensity of the incident light, however, the information about translucent samples is encoded in its phase. In digital holography several techniques can be employed to recover the phase information from one or a number of interferograms. The reconstruction procedure of a hologram is described below.

The intensity image of the object wave interfering with the reference wave described by the complex amplitudes u_{o} and u_{r}, respectively, can be characterized as follows

$$i = |u_{\mathrm{o}} + u_{\mathrm{r}}|^2 = |u_{\mathrm{o}}|^2 + |u_{\mathrm{r}}|^2 + u_{\mathrm{o}}^* u_{\mathrm{r}} + u_{\mathrm{o}} u_{\mathrm{r}}^*. \tag{3.4}$$

In (3.4) there are two so called DC terms (the first two squared terms on the right hand side) and two interference terms $u_{\mathrm{o}}^* u_{\mathrm{r}}$ and $u_{\mathrm{o}} u_{\mathrm{r}}^*$, which carry the phase information. Therefore, the ultimate goal of the hologram reconstruction is to separate one of the interference terms and retrieve the phase. For this purpose a defined phase modulation Φ of the reference wave is introduced so the intensity distribution is modified and described by

$$i = |u_{\mathrm{o}} + u_{\mathrm{r}} \exp(\mathrm{i}\Phi)|^2 = |u_{\mathrm{o}}|^2 + |u_{\mathrm{r}}|^2 + u_{\mathrm{o}}^* u_{\mathrm{r}} \exp(\mathrm{i}\Phi) + u_{\mathrm{o}} u_{\mathrm{r}}^* \exp(\mathrm{i}\Phi). \tag{3.5}$$

Two common optical setups are being used in digital holography: on-axis and off-axis. There are some differences in their optical setups that result in a different hologram reconstruction process. One of the approaches, which the on-axis digital holography uses, is based on the processing of several interference patterns with defined Φ values to

form one phase image of the studied object. This technique is known as phase-shifting interferometry [47]. The main disadvantage of this method is the need to acquire a series of images, which is not suitable for observation of dynamic phenomena. On the other hand, the off-axis holography introduces the phase shift Φ proportional to a spatial coordinate. The proportionality constant (spatial carrier frequency) usually depends on the angle between the object and reference beams. In CCHM the phase shift Φ for the case when diffraction grating grooves are perpendicular to the axis x is expressed as

$$\Phi(x,y) = 2\pi f_{\mathrm{C}} x. \tag{3.6}$$

The introduction of the carrier has an impact on the frequency domain image. The interference terms are shifted by f_{C} and are being separated from the DC terms (see illustrative Fig. 3.3). The reconstruction is described in [48]. The interference pattern

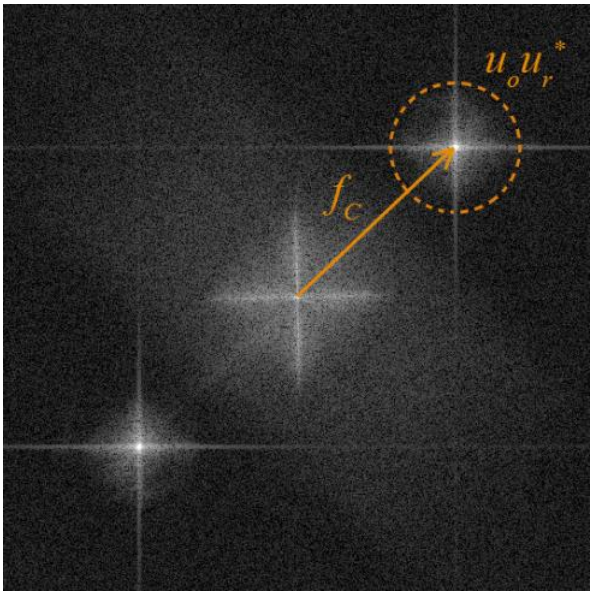

Figure 3.3: Spatial frequency spectrum of the image field. There are two shifted interference terms shifted by the carrier frequency away from the center of the spectrum.

is Fourier transformed and windowing operation is applied on one of the interference terms while the center of the window is at the known carrier frequency f_{C}. This point is then set to be the frequency origin. To suppress Gibb's phenomenon [49] an apodization function is applied on the windowed spectrum. The complex amplitude is computed by inverse Fourier transform and the image amplitude and phase are derived as modulus and argument of the complex amplitude, respectively. This holographic technique allows observation of dynamic phenomena in real time because only one fringe pattern is used for the reconstruction.

3.3 Image formation in CCHM

The basic theory of image formation in CCHM is well described in the work by Chmelik [12]. The derivation of expressions for imaging through scattering media is therefore mainly based on his work.

According to Wolf [50], any arbitrary complex amplitude representation $u(\mathbf{q})$ of a monochromatic wave satisfying Helmholtz equation can be expressed as a superposition of plane waves

$$u(\mathbf{q}) = \iint_{-\infty}^{\infty} U(\mathbf{K}_\mathrm{t}) \exp(2\pi \mathrm{i}\mathbf{K}\cdot\mathbf{q}) \mathrm{d}^2\mathbf{K}_\mathrm{t}, \tag{3.7}$$

where $\mathbf{q} = (\mathbf{q}_\mathrm{t},z) = (x,y,z)$ is a position vector in a Cartesian coordinate system, $U(\mathbf{K}_\mathrm{t})$ is an angular spectrum. Majority of the theory is derived in the spatial frequency domain, therefore, the non-standard reduced wave vector $\mathbf{K} = (\mathbf{K}_\mathrm{t},K_z) = (K_x,K_y,K_z)$ is used. Its transverse components $\mathbf{K}_\mathrm{t}$ acquire the meaning of spatial frequencies. For a wave propagating in the z axis direction $K_z = \sqrt{K^2 - K_\mathrm{t}^2}$ holds. The wave number is defined as $|\mathbf{K}| = K = 1/\lambda = n/\lambda_\mathrm{v}$, where λ is a wavelength in a medium with the refractive index n, λ_v is the wavelength in a vacuum. Evanescent waves are assumed to be decaying too quickly to contribute to the far-field, which means that they are neglected by assuming $U(\mathbf{K}_\mathrm{t}) = 0$ for $K_\mathrm{t} > K$. The angular spectrum can be expressed according to (3.7) as

$$U(\mathbf{K}_\mathrm{t}) = \iint_{-\infty}^{\infty} u(\mathbf{q}) \exp(-2\pi \mathrm{i}\mathbf{K}\cdot\mathbf{q}) \mathrm{d}^2\mathbf{q}_\mathrm{t}. \tag{3.8}$$

Scattering of a primary wave with an angular spectrum $U(\mathbf{K}_\mathrm{t})$ by an object under assumption of a linear and elastic scattering can be described as a scattering of individual plane wave components of the primary wave and a superposition of resulting spectra. The angular spectrum $U'(\mathbf{K'}_\mathrm{t})$ of the scattered field by an object is then expressed by the integral

$$U'(\mathbf{K'}_\mathrm{t}) = \iint_{-\infty}^{\infty} \mathcal{S}(\mathbf{K'},\mathbf{K}) U(\mathbf{K}_\mathrm{t}) \mathrm{d}^2\mathbf{K}_\mathrm{t}, \tag{3.9}$$

where $\mathcal{S}(\mathbf{K'},\mathbf{K})$ is the scattering function of the object. The integration is allowed by the linearity assumption and due to the elasticity of the scattering $K' = K$. In general, when a light wave undertakes several collisions when passing an object, i.e. multiple scattering occurs, it may not be possible to express the function $\mathcal{S}(\mathbf{K'},\mathbf{K})$ in the analytical form. Therefore suppose, that the light is only singly scattered by the object. In this case the scattering function has following form:

$$\mathcal{S}(\mathbf{K'},\mathbf{K}) = C_0(\mathbf{K},\mathbf{Q}) T(\mathbf{Q}), \tag{3.10}$$

where $\mathbf{Q} = (X,Y,Z) = \mathbf{K'} - \mathbf{K}$ is the scattering vector,

$$T(\mathbf{Q}) = \iiint_{-\infty}^{\infty} t(\mathbf{q}) \exp(-2\pi \mathrm{i}\mathbf{Q}\cdot\mathbf{q}) \mathrm{d}^3\mathbf{q} \tag{3.11}$$

is the Fourier transform of the scattering potential $t(\mathbf{q})$ of the object and $C_0(\mathbf{K},\mathbf{Q})$ is a geometric factor.

A planar object, characterized by a transmission function[2] $t_\mathrm{t}(\mathbf{q}_\mathrm{t})$, satisfies the condition of the single scattering, and for the scattering potential it holds

$$t(\mathbf{q}_\mathrm{t},z) = t_t(\mathbf{q}_\mathrm{t})\delta(z) \text{ and simultaneously } C_0 = 1, \tag{3.12}$$

where δ denotes the Dirac delta function.

Scattering potential can be derived for a volume object as well, but the scattering has to be weak or the object has to be imaged only by ballistic light[3]. For that case the following expression was derived by Wolf [51] under the first Born approximation

$$t(\mathbf{q}) = \mathrm{i}\pi[n^2(\mathbf{q}) - 1] \text{ and simultaneously } C_0(\mathbf{K},\mathbf{Q}) = \frac{K^2}{K_z + Z}, \tag{3.13}$$

where $n(\mathbf{q})$ is a refractive index distribution.

The angular spectrum of a light wave is also transformed by an imaging system. In [36, Sec. 9.5] it is shown that in the case of a stigmatic imaging within an isoplanatic region of a system the transition from the object to the image is equivalent to the action of a linear filter. When the output plane is optically conjugated with the object plane, then for the angular spectra of the object and image wave holds

$$U_\mathrm{i}(\mathbf{K}_\mathrm{t}) = P_\mathrm{T}(\mathbf{K})U_\mathrm{o}(\mathbf{K}_\mathrm{t}), \tag{3.14}$$

where the filter function P_T describes the transfer of the object wave angular spectrum U_o by an imaging system. U_i denotes the angular spectrum of the image wave. According to [12] for a rotationally symmetrical aplanatic system a pupil function P_T takes on the following form:

$$P_\mathrm{T}(\mathbf{K}) = \sqrt{\frac{K}{K_z}}\mathrm{circ}\left(\frac{K\cos\alpha}{K_z}\right) = \sqrt{\frac{K}{K_z}}\mathrm{circ}\left(K_\mathrm{t}\frac{\lambda_\mathrm{v}}{\mathrm{NA}}\right), \tag{3.15}$$

where the $\mathrm{circ}(x)$ function is defined as follows

$$\mathrm{circ}(x) = \begin{cases} 1, & \text{for } x < 1, \\ \frac{1}{2}, & \text{for } x = 1, \\ 0, & \text{for } x > 1. \end{cases} \tag{3.16}$$

[2] Transmission function is a ratio of the scattered wave complex amplitude right behind the object and the incident wave complex amplitude.

[3] It is the light that is not angularly disturbed by the medium it passes through.

3.3.1 Imaging of a point object through a scattering layer

This subsection describes the imaging theory of the object behind a planar scattering layer. Solutions derived in this subsection also explain experiments mentioned in Chap. 4. Basics of the theory are explained in [12, Chap. 8] and further derivations are based on this publication.

In the further mathematical and physical investigation of the problem, a linearity of the scattering layer is assumed. That means, the scattering layer can be split into subcomponents, the imaging process can be carried out individually for each subcomponent producing an image, and then to get the final result, the partial images are superposed. A scattering layer, positioned at the distance z_D from the specimen plane (S), can be generally decomposed into diffraction gratings with transmission functions $t_\mathrm{D}(\mathbf{q};z_\mathrm{D},\mathbf{G}_\mathrm{t})$, which allow to pass only one transverse spatial frequency $\mathbf{G}_\mathrm{t}=(G_\mathrm{x},G_\mathrm{y})$ (see [41]). According to (3.12), the scattering potential of such a grating is expressed in the form

$$t_\mathrm{D}(\mathbf{q};z_\mathrm{D},\mathbf{G}_\mathrm{t})=t_\mathrm{t}(\mathbf{q}_\mathrm{t})\delta(z-z_\mathrm{D})=\exp(2\pi\mathrm{i}\mathbf{G}_\mathrm{t}\cdot\mathbf{q}_t)\delta(z-z_\mathrm{D})\text{ and }C_0=1. \tag{3.17}$$

The derivation follows the schematic shown in Fig. 3.4. It depicts a distortion of

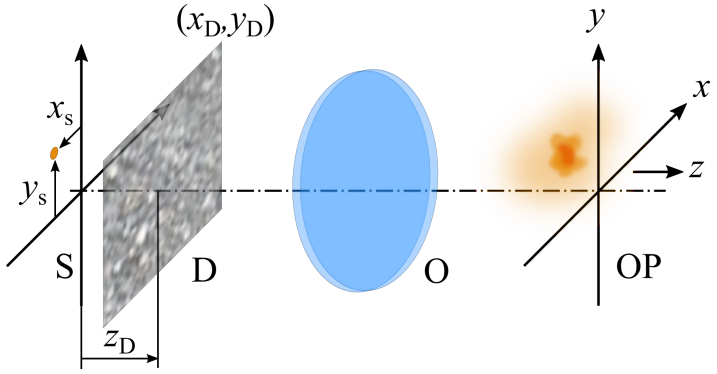

Figure 3.4: Schematic of the model used in the derivation of expression for imaging through scattering medium. S – specimen plane, D – scattering layer, O – objective lens, OP – output plane.

a point object imaged through a scattering layer (D). First suppose, a point object positioned at coordinates $\mathbf{q}_\mathrm{st}=(x_\mathrm{s},y_\mathrm{s})$ in the object plane with the scattering potential

$$t_\mathrm{o}(x_\mathrm{s},y_\mathrm{s},z)=\delta(x-x_\mathrm{s})\delta(y-y_\mathrm{s})\delta(z)\text{ and }C_0=1, \tag{3.18}$$

from which the scattering function for a point object can be derived using (3.11) and (3.10) as

$$\mathcal{S}_\mathrm{o}(\mathbf{K}',\mathbf{K})=\exp[-2\pi\mathrm{i}(\mathbf{K}'_\mathrm{t}-\mathbf{K}_\mathrm{t})\cdot\mathbf{q}_\mathrm{st}]. \tag{3.19}$$

The point object is illuminated through the Köhler illumination system by a fictitious coherent point source that generates a plane wave with a reduced wave vector $\mathbf{K}$ in the object space. The angular spectrum, which the illumination system is able to transfer, is limited by the pupil function P_C and the point source radiates with an amplitude $\sqrt{i(\mathbf{K})}$, then with respect to (3.8) and (3.14), the angular spectrum of the

plane wave is described by

$$U(\mathbf{K}'_{\mathrm{t}}) = \sqrt{i(\mathbf{K})}P_{\mathrm{C}}(\mathbf{K})\delta(K'_{\mathrm{x}} - K_{\mathrm{x}})\delta(K'_{\mathrm{y}} - K_{\mathrm{y}}). \tag{3.20}$$

When the collector lens and the condenser form an aplanatic system, the pupil function P_{C} can be specified by (3.15). The angular spectrum of the wave behind the point object is expressed after substitution of (3.19) and (3.20) into (3.9) by

$$U(\mathbf{K}'_{\mathrm{t}}) = \sqrt{i(\mathbf{K})}P_{\mathrm{C}}(\mathbf{K})\exp[-2\pi\mathrm{i}(\mathbf{K}'_{\mathrm{t}} - \mathbf{K}_{\mathrm{t}})\cdot\mathbf{q}_{\mathrm{st}}]. \tag{3.21}$$

First, a partial result for scattering by the planar layer of single frequency is obtained and then a superposition over all frequency components of the layer is carried out. The scattering function for the single frequency layer can be obtained by substituting (3.17) into (3.11) and then the resulted expression into (3.10). Then it has the following form

$$\mathcal{S}_{\mathrm{G}}(\mathbf{K}'',\mathbf{K}') = \delta(K''_{\mathrm{x}} - K'_{\mathrm{x}} - G_{\mathrm{x}})\delta(K''_{\mathrm{y}} - K'_{\mathrm{y}} - G_{\mathrm{y}})\exp[-2\pi\mathrm{i}(K''_{\mathrm{z}} - K'_{\mathrm{z}})z_{\mathrm{D}}]. \tag{3.22}$$

Propagation of the light wave through this layer transforms the angular spectrum according to (3.9) as

$$U_{\mathrm{G}}(\mathbf{K}''_{\mathrm{t}}) = U(\mathbf{K}''_{\mathrm{t}} - \mathbf{G}_{\mathrm{t}})\exp[-2\pi\mathrm{i}(K''_{\mathrm{z}} - K'_{\mathrm{z}})z_{\mathrm{D}}]. \tag{3.23}$$

Expression (3.21) can be substituted into this function to obtain

$$U_{\mathrm{G}}(\mathbf{K}''_{\mathrm{t}}) = \sqrt{i(\mathbf{K})}P_{\mathrm{C}}(\mathbf{K})\exp[-2\pi\mathrm{i}(\mathbf{K}''_{\mathrm{t}} - \mathbf{G}_{\mathrm{t}} - \mathbf{K}_{\mathrm{t}})\cdot\mathbf{q}_{\mathrm{st}}]\exp[-2\pi\mathrm{i}(K''_{\mathrm{z}} - K'_{\mathrm{z}})z_{\mathrm{D}}], \tag{3.24}$$

which in the case of low numerical apertures ($K''^2_{\mathrm{t}}, G^2_{\mathrm{t}} \ll K_0^2$) can be rewritten using parabolic approximation

$$K''_{\mathrm{z}} - K'_{\mathrm{z}} \approx -\frac{\mathbf{K}'_{\mathrm{t}}\cdot\mathbf{G}_{\mathrm{t}}}{K_0} + \frac{G_{\mathrm{t}}^2}{2K_0}, \tag{3.25}$$

in the following form:

$$U_{\mathrm{G}}(\mathbf{K}''_{\mathrm{t}}) = \sqrt{i(\mathbf{K})}P_{\mathrm{C}}(\mathbf{K}) \times \exp\left\{-2\pi\mathrm{i}\left[\left(\frac{G_{\mathrm{t}}^2}{2K_0} - \mathbf{K}''_{\mathrm{t}}\cdot\frac{\mathbf{G}_{\mathrm{t}}}{K_0}\right)z_{\mathrm{D}} + (\mathbf{K}''_{\mathrm{t}} - \mathbf{G}_{\mathrm{t}} - \mathbf{K}_{\mathrm{t}})\cdot\mathbf{q}_{\mathrm{st}}\right]\right\}. \tag{3.26}$$

Finally the angular spectrum is propagated trough the imaging system to the output plane by means of (3.14) and then the complex amplitude of the wave in the point $\mathbf{q}_{\mathrm{t}}$

of the image plane for the illumination vector $\mathbf{K}$ can be derived using (3.7)

$$u_{\mathrm{o}}(\mathbf{q}_{\mathrm{t}};\mathbf{K}_{\mathrm{t}}) = \sqrt{i(\mathbf{K})}P_{\mathrm{C}}(\mathbf{K})\exp\left\{2\pi\mathrm{i}\left[(\mathbf{G}_{\mathrm{t}}+\mathbf{K}_{\mathrm{t}})\cdot\mathbf{q}_{\mathrm{st}} - \frac{G_{\mathrm{t}}^2}{2K_0}z_{\mathrm{D}}\right]\right\} \times \iint_{-\infty}^{\infty} P_{\mathrm{T}}(\mathbf{K''})\exp\left[2\pi\mathrm{i}\mathbf{K}_{\mathrm{t}}''\cdot\left(\mathbf{q}_{\mathrm{t}}-\mathbf{q}_{\mathrm{st}}+\frac{\mathbf{G}_{\mathrm{t}}}{K_0}z_{\mathrm{D}}\right)\right]\mathrm{d}^2\mathbf{K}_{\mathrm{t}}''. \quad (3.27)$$

This expression gives the complex amplitude in the output plane formed by the object arm of the microscope. For the reference arm a simpler expression can be derived because no scattering is happening along the way of the light. The reference arm of the CCHM has a possibility to laterally shift the objective. The translation of the objective causes the reference field to be shifted by the vector $\mathbf{q}_{\mathrm{f}}$. The position vector $\mathbf{q}_{\mathrm{t}}$ is replaced by $\mathbf{q}_{\mathrm{t}} - \mathbf{q}_{\mathrm{f}}$ and then the relation has the following form:

$$u_{\mathrm{r}}(\mathbf{q}_{\mathrm{t}};\mathbf{K}_{\mathrm{t}}) = \sqrt{i(\mathbf{K})}P_{\mathrm{C}}(\mathbf{K})P_{\mathrm{T}}(\mathbf{K})\exp(2\pi\mathrm{i}\mathbf{K}_{\mathrm{t}}\cdot(\mathbf{q}_{\mathrm{t}}-\mathbf{q}_{\mathrm{f}})). \quad (3.28)$$

According to [12], the reconstructed holographic complex signal of a point object is for the case of the incoherent illumination given by the integration over $\mathbf{K}$. A broad and monochromatic source is now considered, so the integration over K_{z} is left out, then signal is expressed as

$$w(\mathbf{q}_{\mathrm{t}};\mathbf{G}_{\mathrm{t}}) = \iint_{-\infty}^{\infty} u_{\mathrm{o}}(\mathbf{q}_{\mathrm{t}};\mathbf{K}_{\mathrm{t}})u_{\mathrm{r}}^{*}(\mathbf{q}_{\mathrm{t}};\mathbf{K}_{\mathrm{t}})\mathrm{d}^2\mathbf{K}_{\mathrm{t}}. \quad (3.29)$$

In the parabolic approximation that has already been used before, $K_{\mathrm{z}} \approx K$, which simplifies expressions for pupil functions $P_{\mathrm{C}}(\mathbf{K})$ and $P_{\mathrm{T}}(\mathbf{K})$ and leaves them dependent only on the transverse spatial frequencies $\mathbf{K}_{\mathrm{t}}$. A substitution of equations (3.27) and (3.28) into (3.29) gives

$$w(\mathbf{q}_{\mathrm{t}};\mathbf{q}_{\mathrm{st}},\mathbf{G}_{\mathrm{t}},z_{\mathrm{D}}) = \exp\left[2\pi\mathrm{i}\left(\mathbf{G}_{\mathrm{t}}\cdot\mathbf{q}_{\mathrm{st}} - \frac{G_t^2}{2K_0}z_{\mathrm{D}}\right)\right] \times \iint_{-\infty}^{\infty} S_{\mathrm{t}}^{*}(\mathbf{K}_{\mathrm{t}})\exp[-2\pi\mathrm{i}\mathbf{K}_{\mathrm{t}}\cdot(\mathbf{q}_{\mathrm{t}}-\mathbf{q}_{\mathrm{st}}-\mathbf{q}_{\mathrm{f}})]\mathrm{d}^2\mathbf{K}_{\mathrm{t}} \times \iint_{-\infty}^{\infty} P_{\mathrm{t}}(\mathbf{K}_{\mathrm{t}}'')\exp\left[2\pi\mathrm{i}\mathbf{K}_{\mathrm{t}}''\cdot\left(\mathbf{q}_{\mathrm{t}}-\mathbf{q}_{\mathrm{st}}+\frac{\mathbf{G}_{\mathrm{t}}}{K_0}z_{\mathrm{D}}\right)\right]\mathrm{d}^2\mathbf{K}_{\mathrm{t}}'', \quad (3.30)$$

where S_{t} is a parabolic approximation of $S(\mathbf{K}) = i(\mathbf{K})|P_{\mathrm{C}}(\mathbf{K})|^2P_{\mathrm{T}}(\mathbf{K})$. The final expression for the imaging of a point object is obtained by means of the inverse Fourier

transforms s_t, p_t of pupil functions as

$$w(\mathbf{q}_\mathrm{t};\mathbf{q}_\mathrm{st},\mathbf{G}_\mathrm{t},z_\mathrm{D},\mathbf{q}_\mathrm{f}) = \exp\left[2\pi\mathrm{i}\left(\mathbf{G}_\mathrm{t}\cdot\mathbf{q}_\mathrm{st} - \frac{G_\mathrm{t}^2}{2K_0}z_\mathrm{D}\right)\right] \times s_\mathrm{t}^*(\mathbf{q}_\mathrm{t}-\mathbf{q}_\mathrm{st}-\mathbf{q}_\mathrm{f})p_\mathrm{t}\left(\mathbf{q}_\mathrm{t}-\mathbf{q}_\mathrm{st}+\frac{\mathbf{G}_\mathrm{t}}{K_0}z_\mathrm{D}\right). \quad (3.31)$$

The Fourier transforms of the pupil functions $S_\mathrm{t}(\mathbf{K}_\mathrm{t})$ and $P_\mathrm{t}(\mathbf{K}_\mathrm{t})$ can be expressed with the use of the Bessel functions of the first kind as follows

$$p_\mathrm{t}(\mathbf{q}_\mathrm{t}) = \frac{2\mathrm{J}_1(\nu)}{\nu},\ \text{where } \nu = 2\pi\frac{\mathrm{NA}}{\lambda_\mathrm{v}}q_\mathrm{t}, \quad (3.32)$$

$$s_\mathrm{t}(\mathbf{q}_\mathrm{t}) = \frac{2\mathrm{J}_1(\nu_\mathrm{S})}{\nu_\mathrm{S}},\ \text{where } \nu_\mathrm{S} = 2\pi\frac{\mathrm{NA_S}}{\lambda_\mathrm{v}}q_\mathrm{t}, \quad (3.33)$$

where $\mathrm{NA} = n\sin\alpha$ is the numerical aperture of the objective lenses, $\mathrm{NA_S} = n\sin\alpha_\mathrm{S}$ is the minimum of the numerical apertures of the illumination and objective lens. $\mathrm{NA_S}$ directly affects the degree of the spatial coherence. For the coherent illumination $\mathrm{NA_S}\to 0$ and $s_\mathrm{t}(\mathbf{q}_\mathrm{t})\to 1$ for all $\mathbf{q}_\mathrm{t}$. If $\mathrm{NA_S} = \mathrm{NA}$ then the illumination is incoherent.

Now consider a planar layer with a general transmission function $t_\mathrm{D}(\mathbf{q}_\mathrm{t})$, which can be expressed as the superposition

$$t_\mathrm{D}(\mathbf{q}_\mathrm{t}) = \iint_{-\infty}^{\infty} T_\mathrm{D}(\mathbf{G}_\mathrm{t})\exp(2\pi\mathrm{i}\mathbf{G}_\mathrm{t}\cdot\mathbf{q}_\mathrm{t})\mathrm{d}^2\mathbf{G}_\mathrm{t}. \quad (3.34)$$

The imaging of a point object through the general planar layer is then given by

$$w_\mathrm{D}(\mathbf{q}_\mathrm{t};\mathbf{q}_\mathrm{st},z_\mathrm{D},\mathbf{q}_\mathrm{f}) = s_\mathrm{t}^*(\mathbf{q}_\mathrm{t}-\mathbf{q}_\mathrm{st}-\mathbf{q}_\mathrm{f})p_\mathrm{Dt}(\mathbf{q}_\mathrm{t};\mathbf{q}_\mathrm{st},z_\mathrm{D}), \quad (3.35)$$

where p_Dt is

$$p_\mathrm{Dt}(\mathbf{q}_\mathrm{t};\mathbf{q}_\mathrm{st},z_\mathrm{D}) = \iint_{-\infty}^{\infty} T_\mathrm{D}(\mathbf{G}_\mathrm{t})\exp\left[2\pi\mathrm{i}\left(\mathbf{G}_\mathrm{t}\cdot\mathbf{q}_\mathrm{st} - \frac{G_\mathrm{t}^2}{2K_0}z_\mathrm{D}\right)\right] \times p_\mathrm{t}\left(\mathbf{q}_\mathrm{t}-\mathbf{q}_\mathrm{st}+\frac{\mathbf{G}_\mathrm{t}}{K_0}z_\mathrm{D}\right)\mathrm{d}^2\mathbf{G}_\mathrm{t}. \quad (3.36)$$

The imaging of a two-dimensional object defined by the transmission function $t_\mathrm{o}(\mathbf{q}_\mathrm{st})$ through a scattering layer is described by the integral

$$u_\mathrm{2D}(\mathbf{q}_\mathrm{t}) = \iint_{-\infty}^{\infty} t_\mathrm{o}(\mathbf{q}_\mathrm{st})w_\mathrm{D}(\mathbf{q}_\mathrm{t},\mathbf{q}_\mathrm{st};z_\mathrm{D},\mathbf{q}_\mathrm{f})\mathrm{d}^2\mathbf{q}_\mathrm{st}. \quad (3.37)$$

3.3.2 Coherence-gating effect

The possibility to image with completely incoherent illumination by means of interference in CCHM gives rise to the coherence-gating effect. In the reconstruction process of the holographic image, the separation of the interference term causes that only the interfering photons are chosen to form the final reconstructed image. In the case of a coherent source, all the photons (also the scattered and out of focus ones) will interfere and contribute to the final image. However, the decrease in the spatial and temporal coherence reduces the coherence area and length, respectively, which define the coherence volume[4]. Photons arriving to the image space within the coherence volume interfere, but those that hit the output plane outside their coherence area, cannot interfere and, therefore, do not contribute to the reconstructed image.

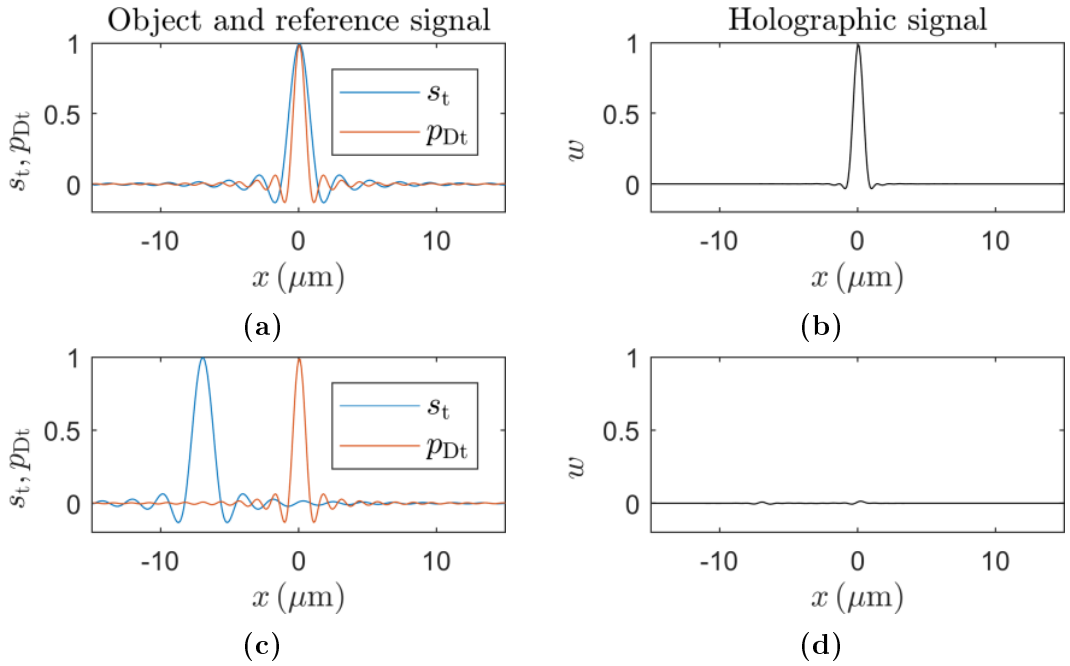

Figure 3.5: Numerical calculations based on (3.29). All figures are cross-sections of the functions $s_t(\mathbf{q}_t)$, $p_{Dt}(\mathbf{q}_t)$ and $w(\mathbf{q}_t)$ for $y = 0$. Figures (a) and (b) illustrate the imaging of a point object with properly aligned microscope arms. Figures (c) and (d) show that no image is formed if the reference arm objective lens is shifted by $x_f = 7\,\mu m$. Computation parameters: NA = 0.50, $NA_S = 0.30$, $\lambda_v = 650\,nm$.

In CCHM the coherence area is defined by the shape of the function $s_t(\mathbf{q}_t)$. In the case of a proper lateral alignment of the microscope arms, images formed by both arms overlay completely in the output plane. Unless a strongly scattering medium is introduced in the object arm, majority of the photons falls in the coherence volume and form the image. Fig. 3.5 illustrates the case of the point object imaging (no diffusive element introduced) for the aligned microscope and for the shifted reference field. In the case of the shifted reference field, the coherence volume is shifted as well (Fig. 3.5c), and no image of a point is generated due to the coherence-gating (Fig. 3.5d).

[4]Coherence volume is defined as the right-angled cylinder with height equal to coherence length and the base is the area of coherence positioned in a plane normal to the direction of propagation [52].

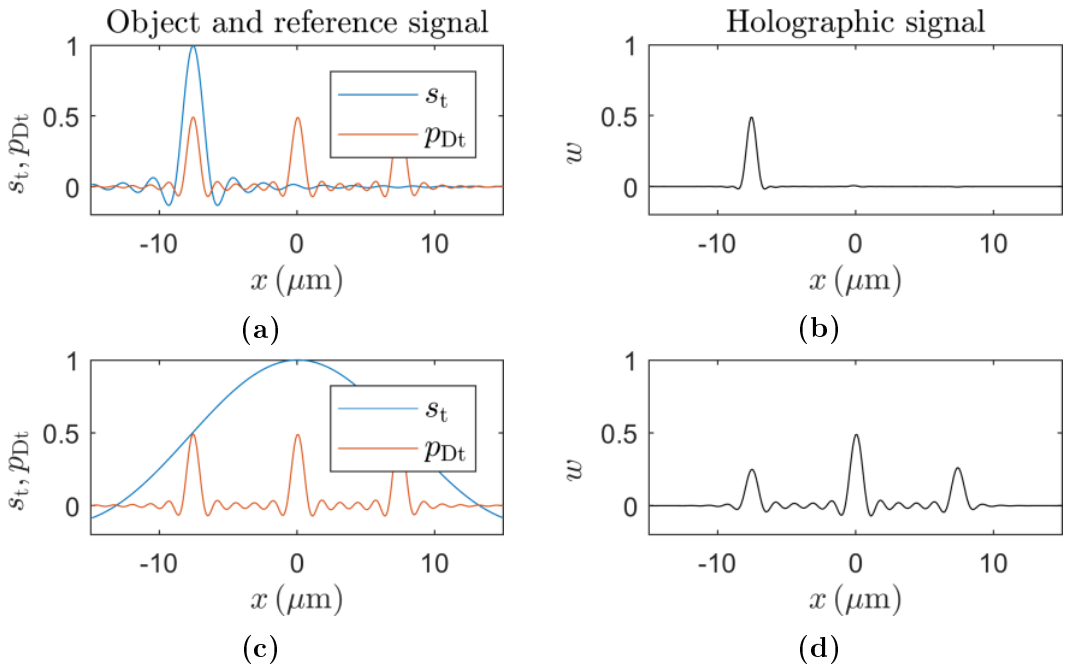

Figure 3.6: Numerical computations of the point object imaging through a single frequency scattering layer demonstrating the coherence-gating effect. In figures (a), (b) $\mathrm{NA_S} = 0.30$ is considered, while a shift $x_\mathrm{f} = -7.6\,\mu\mathrm{m}$ is used to separate one of the diffraction orders. Figures (c) and (d) are calculated for $\mathrm{NA_S} = 0.03$ representing imaging in the coherent light. $\mathrm{NA} = 0.50$ $\lambda_\mathrm{v} = 650\,\mathrm{nm}$

Now consider the case, when a diffraction grating (single frequency layer) is placed behind the point object. A portion of the light passes the grating intact (this light can be called the ballistic light) and some of the field is scattered in the way, that two other shifted images of the point are formed in the output plane (only two diffraction orders are supposed). Due to the coherence-gating effect, one can simply choose, by shifting the reference arm objective, which of the three images will be imaged. See Fig. 3.6a, where a transverse shift $x_\mathrm{f} = -7.6\,\mu\mathrm{m}$ is introduced to the $s_\mathrm{t}(\mathbf{q}_\mathrm{t})$ function.

In the previous examples, an incoherent illumination is assumed ($\mathrm{NA_S} = 0.30$), therefore, the peak of the $s_\mathrm{t}(\mathbf{q}_\mathrm{t})$ function is narrow and provides the filtering effect. Fig. 3.6c shows the broad shape of the $s_\mathrm{t}(\mathbf{q}_\mathrm{t})$ function for $\mathrm{NA_S} = 0.03$, which represents the coherent source. The object and reference arm light is highly mutually coherent which allows also the scattered light to contribute to the final image (see Fig. 3.6d).

3.3.3 Approximative expression for imaging

In Subsec. 3.3.2 it was shown and relations (3.32) and (3.33) suggest, that a change of NA, $\mathrm{NA_S}$ or λ_v can make the main peaks of the functions $s_\mathrm{t}(\mathbf{q}_\mathrm{t})$ and $p_\mathrm{t}(\mathbf{q}_\mathrm{t})$ narrower or broader. For clarification of the analytical results obtained in Subsec. 3.3.1 assume for a moment that $\mathrm{NA}/\lambda_\mathrm{v}$, $\mathrm{NA_S}/\lambda_\mathrm{v} \to \infty$ and imaging is completely stigmatic, hence no aberrations are present. Then following from (3.15) and (3.14) the image of a point object is a point in the output plane, therefore, the functions (3.32) and (3.33) take on the form of the Dirac delta function $s_\mathrm{t}(\mathbf{q}_\mathrm{t}), p_\mathrm{t}(\mathbf{q}_\mathrm{t}) \to \delta(\mathbf{q}_\mathrm{t})$.

By substituting the Dirac delta function into (3.36) it gains the following form

$$p_\mathrm{Dt}(x,y;x_\mathrm{s},y_\mathrm{s},z_\mathrm{D}) \approx \int_{-\infty}^{\infty}\int_{-\infty}^{\infty} T_\mathrm{D}(G_\mathrm{x},G_\mathrm{y}) \exp\left[2\pi\mathrm{i}\left(G_\mathrm{x}x + G_\mathrm{y}y - \frac{G_\mathrm{x}^2+G_\mathrm{y}^2}{2K_0}z_\mathrm{D}\right)\right] \times \delta\left(x - x_\mathrm{s} + \frac{G_\mathrm{x}}{K_0}z_\mathrm{D}\right)\delta\left(y - y_\mathrm{s} + \frac{G_\mathrm{y}}{K_0}z_\mathrm{D}\right)\mathrm{d}G_\mathrm{x}\mathrm{d}G_\mathrm{y}, \quad (3.38)$$

then the filtering property of the delta function [53] can be put into effect and (3.38) reduces to

$$p_\mathrm{Dt}(x,y;x_\mathrm{s},y_\mathrm{s},z_\mathrm{D}) \approx T_\mathrm{D}\left(\frac{K_0}{z_\mathrm{D}}(-x+x_\mathrm{s}),\frac{K_0}{z_\mathrm{D}}(-y+y_\mathrm{s})\right) \times \exp\left\{2\pi\mathrm{i}\frac{K_0}{z_\mathrm{D}}\left[(-x+x_\mathrm{s})x + (-y+y_\mathrm{s})y - \frac{(-x+x_\mathrm{s})^2+(-y+y_\mathrm{s})^2}{2}\right]\right\}. \quad (3.39)$$

The same filtering effect further applies, when $s_\mathrm{t}^*(\mathbf{q}_\mathrm{t} - \mathbf{q}_\mathrm{st} - \mathbf{q}_\mathrm{f})$ in (3.35) is substituted by $\delta(\mathbf{q}_\mathrm{t} - \mathbf{q}_\mathrm{st} - \mathbf{q}_\mathrm{f})$ [5], and the obtained relation is then substituted along with the approximative expression for $p_\mathrm{Dt}(x,y;x_\mathrm{s},y_\mathrm{s},z_\mathrm{D})$ (3.39) into (3.37). The following expression for the imaging of a two-dimensional object is then obtained

$$u_\mathrm{2D}(x,y;x_\mathrm{f},y_\mathrm{f}) \approx t_\mathrm{o}(x-x_\mathrm{f},y-y_\mathrm{f})T_\mathrm{D}\left(-\frac{K_0}{z_\mathrm{D}}x_\mathrm{f},-\frac{K_0}{z_\mathrm{D}}y_\mathrm{f}\right) \times \exp\left[2\pi\mathrm{i}\frac{K_0}{z_\mathrm{D}}\left(-x_\mathrm{f}x - y_\mathrm{f}y - \frac{x_\mathrm{f}^2+y_\mathrm{f}^2}{2}\right)\right]. \quad (3.40)$$

To simplify this expression, the previously used vector notation is introduced. The final equation describing the imaging of a two-dimensional object behind a scattering layer, where the diffraction by the objective and condenser lens apertures is not assumed, has the following form:

$$u_\mathrm{2D}(\mathbf{q}_\mathrm{t};\mathbf{q}_\mathrm{f}) \approx t_\mathrm{o}(\mathbf{q}_\mathrm{t}-\mathbf{q}_\mathrm{f})T_\mathrm{D}\left(-\frac{K_0}{z_\mathrm{D}}\mathbf{q}_\mathrm{f}\right)\exp\left[-2\pi\mathrm{i}\frac{K_0}{z_\mathrm{D}}\left(\mathbf{q}_\mathrm{t}\cdot\mathbf{q}_\mathrm{f} + \frac{|\mathbf{q}_\mathrm{f}|^2}{2}\right)\right]. \quad (3.41)$$

This approximative solution provides an insight into the problem of imaging through a scattering layer and explains several experimental results described in Chap. 4. The

[5] The complex conjugation is left out because of the Dirac delta function properties.

reference field shift parameter $\mathbf{q}_\mathrm{f}$ controls the imaging mode. The zero lateral shift corresponds to the ballistic light imaging and the complex amplitude is modulated by the transmission of the zero-frequency component $T_\mathrm{D}(0,0)$ of the scattering layer. When a non-zero lateral shift of the reference arm objective is introduced, the reconstructed image is formed by the scattered light. In this case the image of the object defined by the transmission function $t_\mathrm{o}(\mathbf{q}_\mathrm{t})$ is due to the scattering process shifted by $\mathbf{q}_\mathrm{f}$. The scattering induced shift can be explained by the simplified illustration in Fig. 3.7.

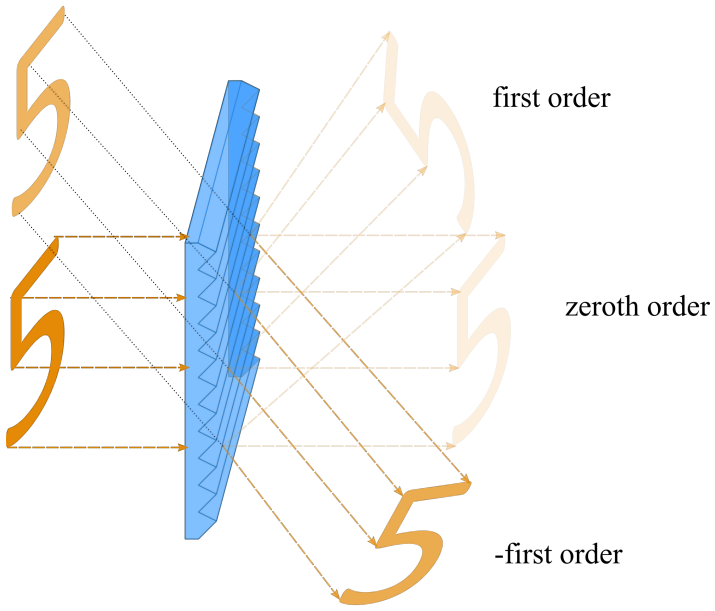

Figure 3.7: The specimen appears to be shifted, when the image formed by the scattered light is back-traced.

The object field is diffracted by the single frequency layer to a particular angular direction (for example − first order), which produces the shifted image in the output plane. By tracing the imaging process in the opposite direction (from the output plane to the specimen), while ignoring the scattering element for a moment, it appears that the specimen is positioned at the different location.

The shift $\mathbf{q}_\mathrm{f}$ also determines, which frequency component of the scattering layer scatters the coherence-gated light, and also a linear phase distortion proportional to $\mathbf{q}_\mathrm{f}$ is present. The modulation $T_\mathrm{D}(-K_0/z_\mathrm{D}\mathbf{q}_\mathrm{f})$ is the property of the scattering medium and can be hardly predicted. However, if the wavelength of the illumination and the distance z_D are known, then at least the linear phase distortion, i.e. the complex exponential term, can be compensated.

3.4 Phase distortion elimination

According to (3.41) a linear phase distortion and a constant phase shift should appear in the image if the reference field is shifted. This conclusion agrees with the experimental data, image of such a distorted phase image is shown in Fig. 3.8. The phase image was acquired by shifting the reference field by 4 µm in the x-axis direction. This section deals with the elimination and the most reliable compensation of the phase distortion.

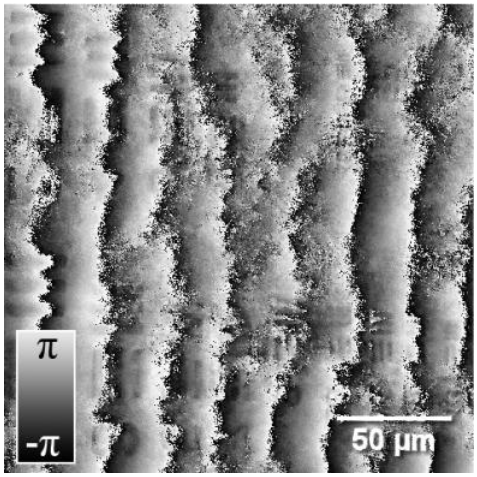

Figure 3.8: Example of the linear phase distortion of the image acquired for a shifted reference field by 4 µm in the x-axis direction. One of the images from experiment described in Subsec. 4.4.1. ($\mathrm{NA_S} = 0.30$, interference filter 650 nm/10 nm full width at half maximum (FWHM), objective lenses 20x/NA = 0.50)

3.4.1 Analytical compensation

The linear phase distortion of the image at a the point $\mathbf{q}_\mathrm{t}$ caused by the complex exponential term $\exp[-2\pi\mathrm{i}K_0/z_\mathrm{D}(\mathbf{q}_\mathrm{t}\cdot\mathbf{q}_\mathrm{f} + |\mathbf{q}_\mathrm{f}|^2/2)]$ on the right hand side of (3.41) can be eliminated by multiplying the complex signal at that point by a complex conjugate of the exponential term. This procedure is derived while assuming the ideal case when $\mathrm{NA}/\lambda_\mathrm{v}$, $\mathrm{NA_S}/\lambda_\mathrm{v} \to \infty$. The situation is however different, when a diffraction by objective and condenser apertures is present. Consider again the model situation of imaging through a diffraction grating like in Fig. 3.6a. The diffraction grating produces a shifted image in the output plane with the peak of the $p_\mathrm{Dt}(\mathbf{q}_\mathrm{t})$ function at the position $\mathbf{q}_\mathrm{t}^\mathrm{max}$ (also peaks of other diffraction orders are present, but the explanation involves just one of them). In this case the approximative expression for image formed is

$$u_\mathrm{2D}(\mathbf{q}_\mathrm{t};\mathbf{q}_\mathrm{t}^\mathrm{max}) \approx t_\mathrm{o}(\mathbf{q}_\mathrm{t}-\mathbf{q}_\mathrm{t}^\mathrm{max})T_\mathrm{D}\left(-\frac{K_0}{z_\mathrm{D}}\mathbf{q}_\mathrm{t}^\mathrm{max}\right) \times \exp\left[-2\pi\mathrm{i}\frac{K_0}{z_\mathrm{D}}\left(\mathbf{q}_\mathrm{t}\cdot\mathbf{q}_\mathrm{t}^\mathrm{max} + \frac{|\mathbf{q}_\mathrm{t}^\mathrm{max}|^2}{2}\right)\right]. \quad (3.42)$$

If the shift $\mathbf{q}_\mathrm{f}$ is during the acquisition of the image chosen the way that the maximum of $s_\mathrm{t}(\mathbf{q}_\mathrm{t})$ is positioned precisely over the local maximum of the function $p_\mathrm{Dt}(\mathbf{q}_\mathrm{t})$ at $\mathbf{q}_\mathrm{t}^\mathrm{max}$, then the phase can be eliminated by the complex conjugate of the exponential term in (3.41) because $\mathbf{q}_\mathrm{f} = \mathbf{q}_\mathrm{t}^\mathrm{max}$.

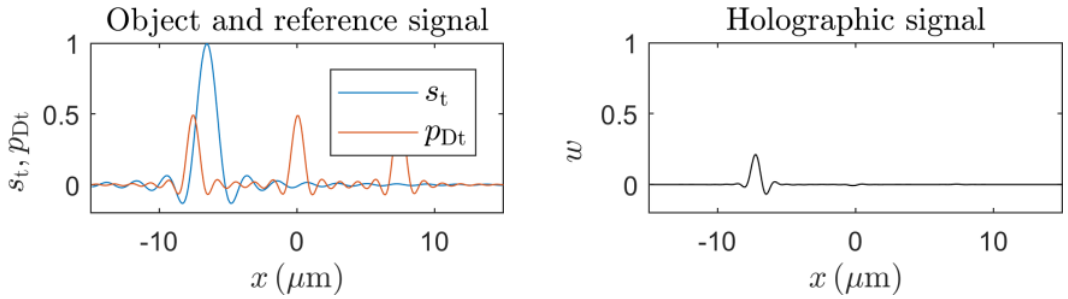

(a) (b)

Figure 3.9: Numerical computations of the point object imaging through a single frequency scattering layer with misaligned peaks of $s_\mathrm{t}(\mathbf{q}_\mathrm{t})$ and $p_\mathrm{Dt}(\mathbf{q}_\mathrm{t})$ functions. $\mathrm{NA_S} = 0.30$, $\mathrm{NA} = 0.50$ $\lambda_\mathrm{v} = 650\,\mathrm{nm}$

However, if the peak center of $s_\mathrm{t}(\mathbf{q}_\mathrm{t})$ is shifted with respect to the local maximum of $p_\mathrm{Dt}(\mathbf{q}_\mathrm{t})$ (see Fig. 3.9a), then (3.41) does not hold. If there is no other peak in the function $p_\mathrm{Dt}(\mathbf{q}_\mathrm{t})$ relatively close and $s_\mathrm{t}(\mathbf{q}_\mathrm{t})$, $p_\mathrm{Dt}(\mathbf{q}_\mathrm{t})$ functions still overlay partially, then resulted maximum of the signal $w(\mathbf{q}_\mathrm{t})$ is lower (see Fig. 3.9b), but the image is still formed by the photons scattered by the same diffraction grating $T_\mathrm{D}(-K_0/z_\mathrm{D}\mathbf{q}_\mathrm{t}^\mathrm{max})$. In the real measurement only $\mathbf{q}_\mathrm{f}$ is known, whereas to compensated the phase distortion the knowledge of $\mathbf{q}_\mathrm{t}^\mathrm{max}$ is required.

Therefore, the analytical phase compensation, based on the knowledge of the reference field shift $\mathbf{q}_\mathrm{f}$, may not remove the linear phase distortion completely.

3.4.2 Iterative compensation

To deal with the imperfect phase compensation, an iterative algorithm based on the Gradient ascent method[6] was designed. The goal is to compensate for the linear phase distortion, and partially compensate for the modulation $T_\mathrm{D}(-K_0/z_\mathrm{D}\mathbf{q}_\mathrm{t}^\mathrm{max})$, and simultaneously ensure the constructive coherent superposition of two complex images for different shifts $u_\mathrm{2D}[\mathbf{q}_\mathrm{t};\mathbf{q}_\mathrm{f} = (0,0)]$ and $u_\mathrm{2D}[\mathbf{q}_\mathrm{t};\mathbf{q}_\mathrm{f} \neq (0,0)]$.

The objective function is defined as follows:

$$J(a,b,c) = \mathrm{mean}_\mathrm{mod}\{u_\mathrm{2D}[\mathbf{q}_\mathrm{t};\mathbf{q}_\mathrm{f} = (0,0)] + u_\mathrm{2D}[\mathbf{q}_\mathrm{t};\mathbf{q}_\mathrm{f} \neq (0,0)]\exp[-\mathrm{i}(ax + by + c)]\}, \tag{3.43}$$

where $\mathrm{mean}_\mathrm{mod}[f(\mathbf{q})]$ function calculates the average value of the modulus of the complex input function $f(\mathbf{q})$, values of $\mathbf{q}$, over which the average modulus is calculated, are confined to the field of view and a, b, c are parameters that are being optimized.

[6] Gradient ascent is a method maximizing an objective function $J(\boldsymbol{\theta})$ with model parameters $\boldsymbol{\theta}$. The maximization is carried out by following the direction of the gradient of the objective function by updating the parameters $\boldsymbol{\theta} = \boldsymbol{\theta} - \eta \cdot \nabla_\theta J(\boldsymbol{\theta})$, η is the step size. [54]

Function $J(a,b,c)$ experiences a lot of local maxima, therefore the initial guess is crucial for the algorithm to converge to the desired solution. The initial guess in the iteration process is based on the analytical compensation described in Subsec. 3.4.1, and then a defined number of iterations is carried out.

3.5 Image synthesis

It is possible to acquire images for various reference field shifts, where in the ideal case each image is formed by the interference of photons scattered by the scattering layer component of a different spatial frequency. Due to the inhomogeneous scattering throughout the field of view, the predominant angular deviation of photons passing through the strongly scattering layer varies for each area of the field. It means that the coherence-gating effect allows to interfere high amounts of photons only in some areas of the whole field of view. The modulus of a holographic signal in an image point is proportional to the number of photons that interfered at that point. According to derivation in [55], a standard deviation of a measured phase in CCHM is inversely proportional to the measured holographic signal modulus. It can be described by the following relation

$$\sigma_{\Phi} \propto \frac{1}{|\mathcal{A}|}\sqrt{I_{\mathrm{o}} + I_{\mathrm{r}}} \tag{3.44}$$

where $|\mathcal{A}|$ denotes the modulus of the reconstructed signal, I_{o} and I_{r} are the object and reference arm intensities in the region of interest. Therefore, areas of higher signal modulus are characterized by lower standard deviation of the phase (I_{o} and I_{r} are assumed to be slowly varying over the field of view). In addition to that, experiments have shown, there are another various phase artifacts and ambiguities in areas of lower signal modulus.

The simplest method to synthesize image using scattered light is to coherently sum compensated images for different objective shifts, each carrying different piece of information about the object. While aiming to create synthetic phase image, the signal modulus of the scattered light serves during superposition as a weighting coefficient. This means, that areas of low amplitude experiencing phase ambiguities have low significance and the final phase image is mostly formed by the phase of areas where more photons interfered during acquisition.

3.6 Measurement scheme

Acquisition of images formed by the scattered light is carried out by shifting the reference arm objective lens in a raster pattern and by recording the hologram for each objective lens shift. This procedure is illustrated in Fig. 3.10, where it is schematically shown that the shifting is executed in steps of 1 µm in the range of ±5 µm in both directions around the central position representing the imaging by the ballistic light (B). The red line in Fig. 3.10 shows how the objective moves during the scanning phase between acquisition positions. One square corresponds to one acquisition position.

Mutual shift of the object and the reference arm fields causes damping of the ballistic light interference and gives rise to the interference of the multiply scattered light, which in the case of a strongly scattering layer dominates.

Without prior knowledge about the scattering layer parameters and its spatial orientation in relation to the object, it is not possible to predict, which values of $\mathbf{q}_\mathrm{f}$ would provide the highest quality image. Due to this fact, acquisition of a large set of images is carried out. Synthesized image is then composed either out of all acquired images or a subset can be used.

CCHM allows to control the range and the step size of the measurement raster pattern. These parameters should be chosen with respect to the sample and the diffuser parameters.

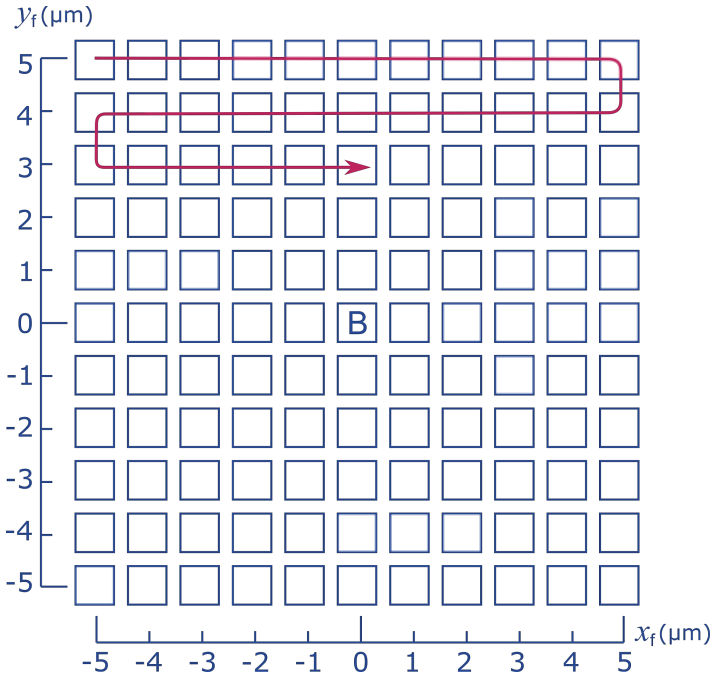

Figure 3.10: Measurement scheme for the acquisition of images formed by scattered light. The reference arm objective lens is being shifted in steps of 1 μm in a raster pattern. Red line with arrow shows the movement of the objective lens between acquisition positions. The letter B in the center denotes the position corresponding to the imaging by ballistic light.

4. Experiments

For the verification purposes, several experiments were carried out proving the analytical results (Sec. 3.3), phase compensation (Sec. 3.4) and image synthesis procedures (Sec. 3.5). Experiments are focused on the coherence-gating effect and its ability to separate ballistic or multiply scattered photons. It is predicted that scattered light should form an image of the object in a similar manner as the ballistic light does. This has been already shown in [24], but the main focus of this work is on the use of scattered light images to create a synthetic image with improved quality. The experimental data are further presented for differently strong diffusers and the results are discussed and explained, some of the data have been presented at the SPIE Photonics Europe conference and are part of the proceeding paper [56].

4.1 Sample used in experiments

A sample, obeying assumptions made along the derivation process of imaging principles in Sec. 3.3, had to be chosen or designed.

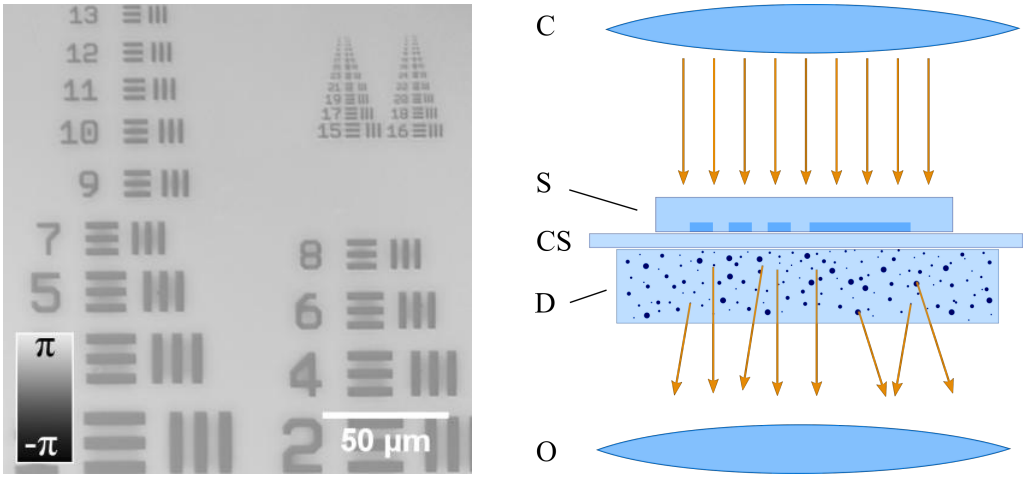

(a) (b)

Figure 4.1: (a) Phase image of the resolution target acquired by CCHM ($NA_S = 0.30$, interference filter 650 nm/10 nm FWHM, objective lenses 20x/NA = 0.50). (b) The sample formed by the phase resolution taret as the specimen (S), coverslip (CS) to separate specimen and diffuser (D), different scatterers were used in experiments. (C) denotes the condenser, and (O) the objective lens of the object arm.

A phase resolution target (similar to USAF 1951 resolution target[1]) was used as

[1]The test target consists of several numbered groups decreasing in size, where each group is composed of six bar elements. The smallest resolvable group determines the resolving power of the imaging system.

a specimen (S). It is manufactured by electron lithography into polymethyl methacrylate resist with the thickness of 0.25 µm (corresponding to the phase shift $0.38\,\pi$ in the experiments). In Fig. 4.1a, there is a phase image of the resolution target, acquired by CCHM. The resolving power of the imaging system can be determined from acquired images of the resolution target, however, the purpose of this thesis is not to provide a quantitative information about resolution. The test target is used because it has a known structure, which makes the evaluation of a proper functionality of image synthesis procedures easier. The diffuser is placed in front of the object and it is separated from the specimen by a coverslip (130 µm thick), the sample setup is shown in Fig. 4.1b. The coverslip defines the distance z_{D} (see Fig. 3.2 and Fig. 3.4). The sample formed by these three elements is then placed into the object arm of the microscope setup as shown in Fig 3.2.

4.2 Coherence-gating effect

First of all, a possibility of CCHM to control the spatial coherence of the illumination, which allows to image a specimen by (practically) a coherent or an incoherent light, is demonstrated. A simple adjustment of the condenser aperture size switches between these two imaging modes. Therefore, it is easy to analyze so called coherence-gate effect and its impact on the image quality.

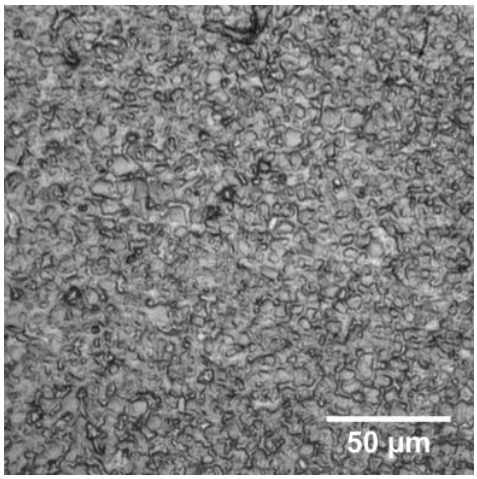

Figure 4.2: Bright-field image of the etched glass surface acquired by CCHM ($\mathrm{NA_S} = 0.30$, interference filter 650 nm/10 nm FWHM, objective lenses 20x/NA = 0.50).

In this case an opaque glass plate was used in place of the diffuser (see Fig. 4.1b). A bright-field image of the glass plate surface is shown in Fig. 4.2. The scattering layer is produced by etching of one of the glass plate surfaces. Depth of the resulted etched structures, determined from the phase image, varies from 0.6 µm to 2.0 µm. The lateral size of the produced grains ranges from tens of micrometers down to several micrometers.

Fig. 4.3 compares the imaging with $\mathrm{NA_S} = 0.30$ corresponding to the spatially incoherent illumination and imaging with $\mathrm{NA_S} = 0.05$, which corresponds to the coherent illumination. Fig. 4.3a shows the phase image of the object examined through the

scattering layer and illuminated by the incoherent light. Despite the fact that minor phase distortions appear, it can be concluded that both the structure and the phase of the image is similar to the image without the scattering layer (Fig. 4.1a) proving the coherence-gating capability of CCHM. The imaging with low NA_S (Fig. 4.3b) is of low quality due to the out of focus light interference. The image experiences major phase distortions, which result in many phase ambiguities, also artifacts caused by diffraction on the condenser aperture is present. Obviously, image in this form is not suitable for QPI applications.

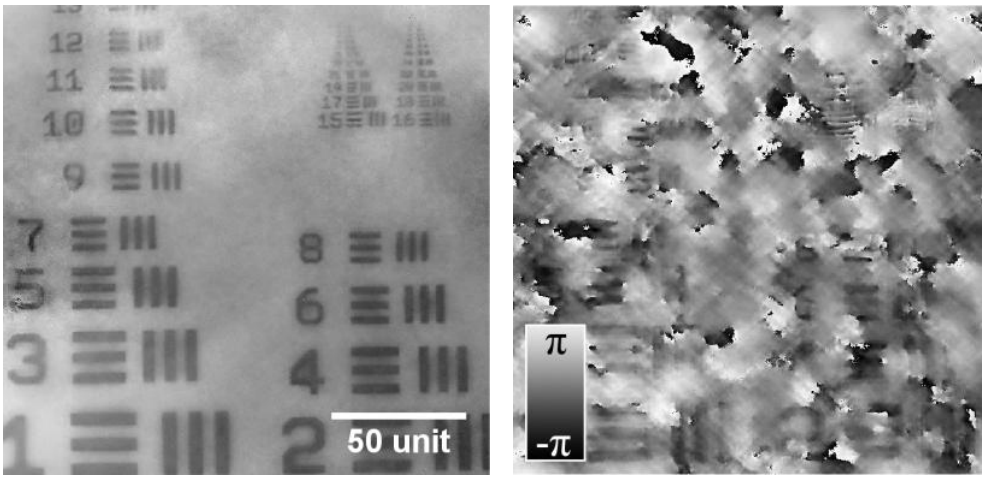

(a) **(b)**

Figure 4.3: Comparison of phase images obtained in the incoherent illumination (a), $NA_S = 0.30$, and the coherent illumination (b), $NA_S = 0.05$, interference filter 650 nm/10 nm FWHM, objective lenses 20x/NA = 0.50. Images correspond to position marked as B in the measurement scheme in Fig. 3.10. Both images are for the purpose of easier recognizability of the resolution target rotated and flipped in relation to the original image.

4.3 Weak diffuser

One of the experiments was carried out with an intentionally scratched and ground coverslip as a scattering layer. Its structure, shown in Fig. 4.4, is relatively coarse. There are areas, where the surface is intact, but also areas with structures of transverse dimensions ranging from several to tens of micrometers. The depth of pits is determined from the phase image of the coverslip. Maximum depth is determined to be about 15 µm.

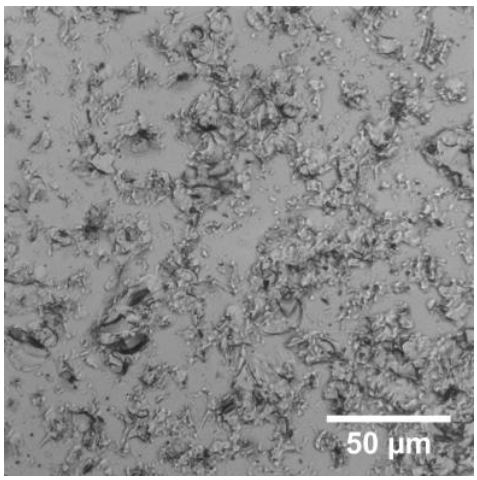

Figure 4.4: Bright-field image of the ground coverslip surface acquired by CCHM ($NA_S = 0.30$, interference filter 650 nm/10 nm FWHM, objective lenses 20x/NA = 0.50).

It may be expected, based on the bright-field image of the ground coverslip (Fig. 4.4), that a large portion of the light will pass the ground coverslip intact. This is proved by an experimental data, which are acquired by the procedure described in Sec. 3.6. The images, for various transverse shifts $\mathbf{q}_f$, are stitched together in Fig. 4.5 to illustrate the phase distortion of the scattered light. An obvious phase ramp, predicted by (3.41) appears only in some of the images, particularly in those acquired for greater field shifts. Based on the theory, the ballistic light, corresponding to the $\mathbf{q}_f = (0,0)$, should not experience any phase distortion. This indicates, that if there is not a significant linear phase distortion in images, which are acquired with non-zero shifts of the reference arm objective, the ballistic light interference dominates.

The amount of the scattered light by a diffusive medium can be analyzed by a comparison of the average signal modulus[2] of acquired images. The measured signal modulus for different shifts without a sample (Fig. 4.6a) provides information about the ballistic component, because no scattering is happening in this case, and all the light is technically ballistic. Any medium introduced to the optical path scatters and absorbs a portion of otherwise ballistic light. The distribution of the light is not uniform over the field of view, but the average value of the signal modulus well demonstrates the amount of light scattered in a particular direction, or if no scattering occurs, the de-

[2]The signal modulus value provided by the CCHM software is defined as a number of gray levels (CCD camera pixel has a 14-bit dynamic range) scale between the value of dark fringe and the value of bright fringe.

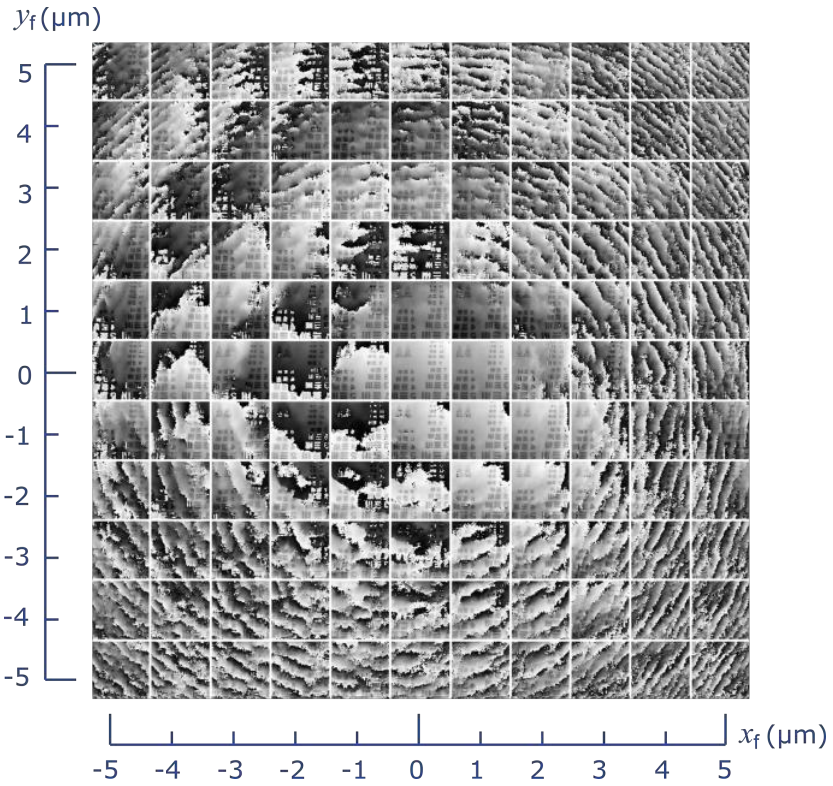

Figure 4.5: The image composed of 121 non-compensated phase images obtained by scanning the objective lens in the reference arm according to the procedure described in Sec. 3.6. The ground coverslip is used as a diffuser.

gree of an overlap of the ballistic signal in the object arm and the reference arm signal. Fig. 4.6b shows that an introduction of a sample lowers the average signal modulus values of the ballistic light image (from 6000 to 4000 in this case). However, it is still about an order higher compared to the images acquired from the scattered light (signal modulus ranges from 150 to 300).

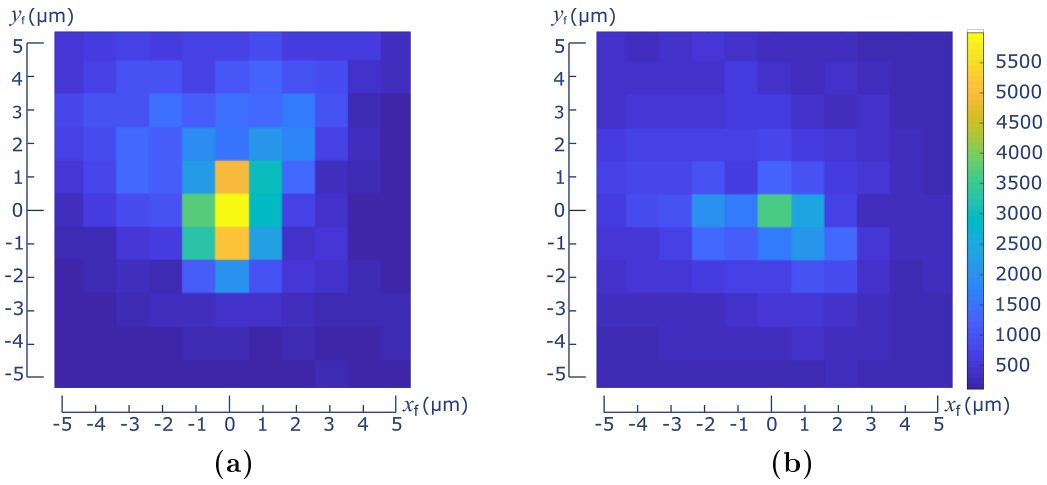

Figure 4.6: (a) Average signal modulus map of acquired images for various shifts without any sample. (b) Average signal modulus map of acquired images for various shifts with resolution target and the ground coverslip as the diffuser. Color scale denotes the dimensionless modulus of the complex signal.

An illustrative explanation, why the ballistic component is more significant even in images acquired for the shifted reference field, is provided by a simple computational model based on (3.35). Consider for a moment, an imaging of a point object through a weakly scattering layer, which is an analogy to this experiment with the ground coverslip. The function $s_{\mathrm{t}}(\mathbf{q}_{\mathrm{t}})$ is modeled according to (3.33) and $p_{\mathrm{Dt}}(\mathbf{q}_{\mathrm{t}}) = p_{\mathrm{Dt}}^{Bal}(\mathbf{q}_{\mathrm{t}}) + p_{\mathrm{Dt}}^{Scat}(\mathbf{q}_{\mathrm{t}})$ is modeled as a superposition of the ballistic light $p_{\mathrm{Dt}}^{Bal}(\mathbf{q}_{\mathrm{t}})$ and scattered light $p_{\mathrm{Dt}}^{Scat}(\mathbf{q}_{\mathrm{t}})$ component. The function $p_{\mathrm{Dt}}^{Bal}(\mathbf{q}_{\mathrm{t}})$ is modeled as the Bessel function of the first kind (3.32), with the amplitude of the main peak being 0.9 and the scattered light part $p_{\mathrm{Dt}}^{Bal}(\mathbf{q}_{\mathrm{t}})$ is modeled as a uniform random distribution in the amplitude interval (0,0.3). Random phase deviations are not in this illustrative case assumed. A cross-section for $y = 0$ of the model situation is shown in Fig. 4.7a, where the peak of the ballistic image of the point (yellow line) is much higher than the scattered light amplitude (red line). If the reference field (i.e the function $s_{\mathrm{t}}(\mathbf{q}_{\mathrm{t}})$) is shifted in a way that ballistic component and $s_{\mathrm{t}}(\mathbf{q}_{\mathrm{t}})$ function does not overlap completely, then the resulted holographic signal $w(\mathbf{q}_{\mathrm{t}})$ is mostly formed by the damped, but still dominant, interference of ballistic photons. The problem of such an image is a presence of the second shifted ghost image formed by the scattered photons. Image in Fig. 4.8b is acquired when the reference field is shifted by $\mathbf{q}_{\mathrm{f}} = (0, 3\,\mu\mathrm{m})$, therefore, there is a ghost image shifted by $-3\,\mu\mathrm{m}$ in the direction of the axis y. In our microscope system, the

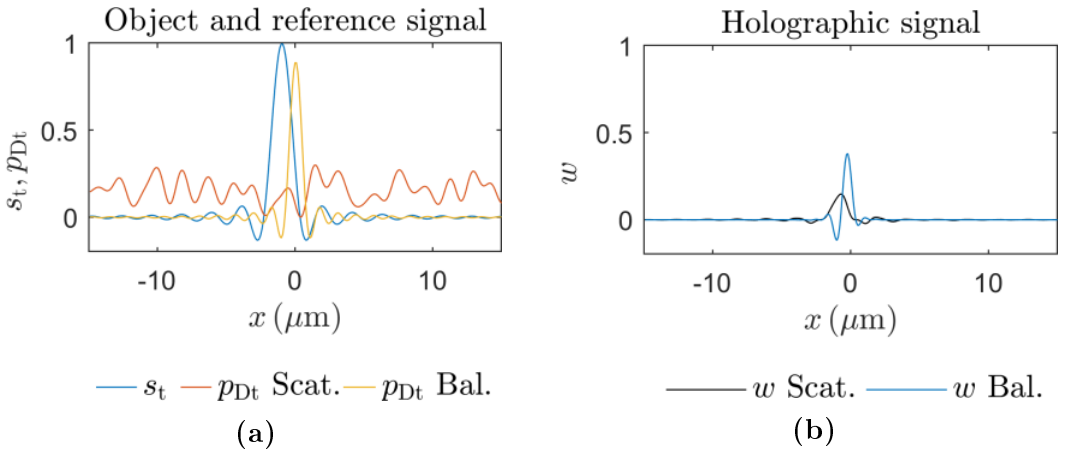

Figure 4.7: Simulated situation of the imaging of a point object through a *weakly* scattering layer. (a) The object arm signal is split into two components: ballistic and the component induced by the scattering process. (b) Image of the point formed predominantly by the ballistic light interference. Parameters: $\mathrm{NA_S} = 0.30$, $\mathrm{NA} = 0.50$ $\lambda_{\mathrm{v}} = 650\,\mathrm{nm}$.

$s_{\mathrm{t}}(\mathbf{q}_{\mathrm{t}})$ is due to optical aberrations asymmetric and also side lobes has higher amplitude as the approximative expression (3.33). This fact causes the dominance of the ballistic light even for a few particular reference field shifts, where the scattered light would be in the ideal case more significant.

As mentioned before, the ground coverslip used, but also weak diffusers in general, allow to pass a large portion of the ballistic light. In majority of practical cases involving the imaging through weak diffusers, the coherence gated ballistic light is sufficient to produce a high quality quantitative phase image of a specimen. The dominance of the

ballistic light also does not allow to use proposed method to synthesize an image using images formed by shifting the reference field. Therefore, it seems that in the case of imaging through a weakly scattering medium, the best approach is to use only single image formed by the ballistic light. The image for the shift $\mathbf{q}_{\mathrm{f}} = (0,0)$ is shown in Fig. 4.8a. Its quality is almost identical with the image in Fig. 4.1a acquired without any diffuser.

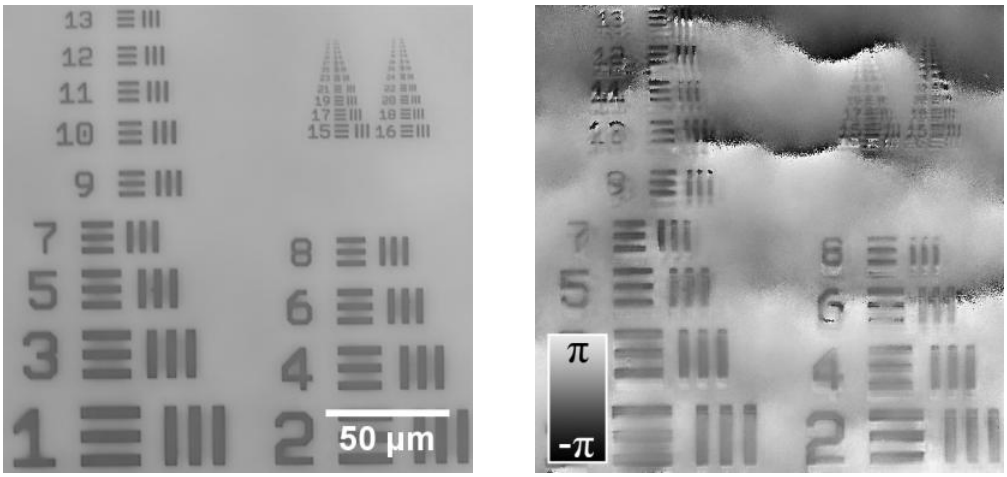

(a) **(b)**

Figure 4.8: (a) The ballistic light phase image of the phase resolution target through weakly scattering layer (scratched cover slip) and (b) the phase acquired for shift $\mathbf{q}_{\mathrm{f}} = (0, 3\,\mu\mathrm{m})$ ($\mathrm{NA_S} = 0.30$, interference filter 650 nm/10 nm FWHM, objective lenses 20x/NA = 0.50).

4.4 Strong planar diffuser

The diffuser used in the series of experiments explained in this section is the etched glass plate. Its properties are described in Sec. 4.2, however a strength of the scattering varies over the surface of the glass plate, therefore every experiment can provide slightly different outcome. A lot of data have been acquired using various experimental arrangements of the resolution target and the etched glass plate under different microscope settings. In order to explain main concepts of the phase distortion correction and the image synthesis process, only a limited amount of the data has been chosen to be presented in this section.

4.4.1 Illumination by condenser lenses

The measurement was again carried out according to the procedure described in Sec. 3.6. The central (ballistic) image of this measurement was also used in Sec. 4.2 to demonstrate the coherence-gating effect. The set of images in Fig. 4.9 shows how the field at the output plane, acquired with a shifted reference arm objective lens, experiences linear phase distortion. Even the images for 1 µm shifts have visible phase jumps, however the ballistic light component is still present, and in some images dominant.

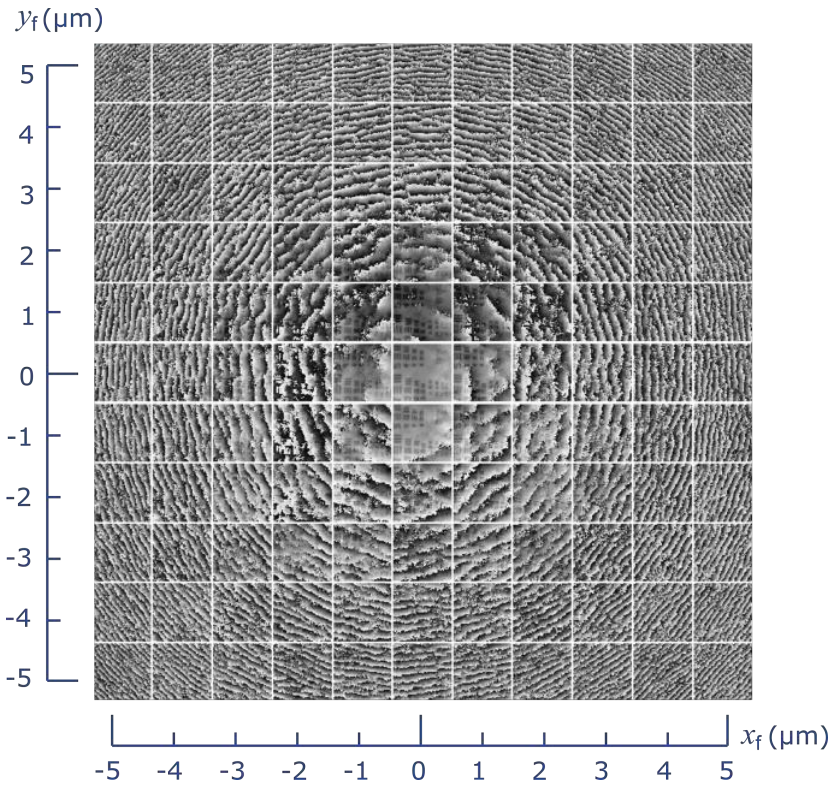

Figure 4.9: Composed image out of 121 phase images obtained by scanning the objective lens in the reference arm according to the procedure described in Sec. 3.6 for the etched glass plate experiment with $\mathrm{NA_S} = 0.30$.

Fig. 4.10 in comparison with Fig. 4.6a shows that the majority of the light is scattered by the etched glass plate, i.e. the ballistic central image has a lot lower

average signal modulus (about 1000) than the one without a sample. When the signal modulus of the ballistic image is lower, also the ballistic component in the images acquired with shifted field is expected to be a lot less significant. This assumption is confirmed by the fact that visible fringes appear as soon as the reference objective lens is transversely shifted.

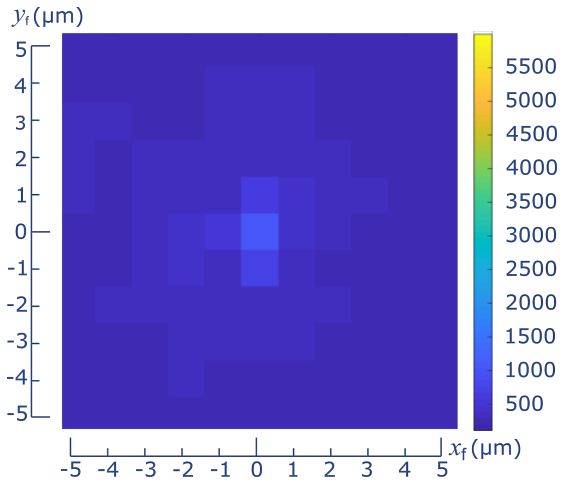

Figure 4.10: Average signal modulus map of acquired images for various shifts with resolution target and the etched glass plate as the diffuser ($\mathrm{NA_S} = 0.30$). Color scale denotes the dimensionless modulus of the complex signal.

In Fig. 4.11, there is the simulated situation of a point object imaging through strongly scattering planar layer. It considers a case when the ballistic image average signal modulus is of the same order as the average signal modulus of the image formed by scattered light (see Fig. 4.11a).

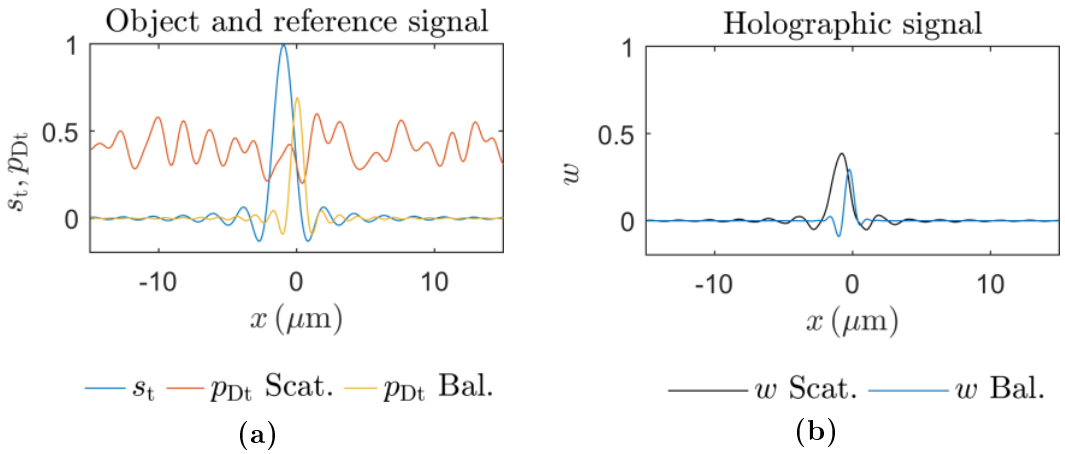

Figure 4.11: Simulated situation of the imaging of a point object through a *strongly* scattering layer. (a) The object arm signal is split into two components: ballistic and the component induced by the scattering process. (b) Image of the point formed by the interference. Parameters: $\mathrm{NA_S} = 0.30$, $\mathrm{NA} = 0.50$ $\lambda_v = 650\,\mathrm{nm}$.

The functions $s_t(\mathbf{q}_t)$ and $p_{Dt}(\mathbf{q}_t)$ are modeled in the same way as in Sec. 4.3. The amplitude of the $p_{Dt}^{Bal}(\mathbf{q}_t)$ peak is 0.7 and $p_{Dt}^{Scat}(\mathbf{q}_t)$ is again uniform random distribution in the amplitude interval (0.2,0.6). The introduction of the transverse reference field

shift $\mathbf{q}_f$ causes a damping of the ballistic holographic signal below the scattered light signal.

If the scattered light component is significantly dominant over the ballistic light, then (3.41) holds, and the phase compensation of the complex exponential can be applied. In Subsec. 3.4.1 and 3.4.2 it is predicted that a relatively undistorted image can be retrieved by the phase correction. The iterative algorithm was applied to all the images of acquired set, while the initial guess was based on the analytical solution. Fig. 4.12 shows results of the compensation procedure. The vast majority of images is free of linear phase distortion, however, the compensation fails when there is still a significant amount of the ballistic light interference in the image. These images, where the procedure failed, have visible linear phase ramp (fringes) in them.

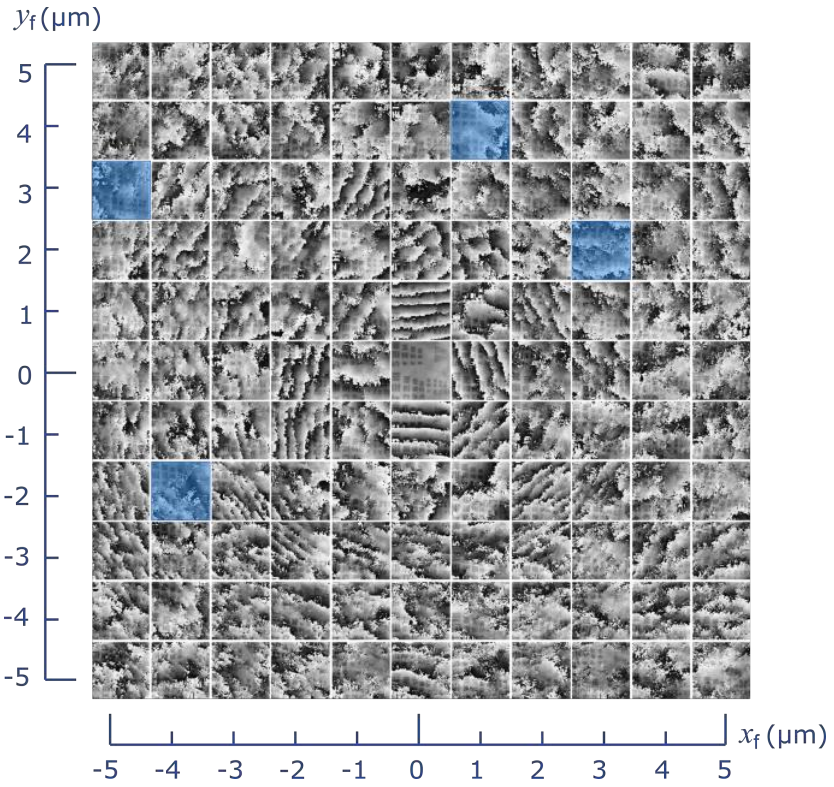

Figure 4.12: Composed image of compensated phase images recorded according to the measurement scheme described in Sec. 3.6. Phase compensation used was based on analytical calculations and for more precise phase flattening also the gradient ascent based optimization was used.

Fig. 4.13 shows enlarged examples of compensated images marked by the blue color in Fig. 4.12. The phase is even after the compensation experiencing major distortions, jumps and ambiguities. A careful comparison of the top row phase images with the bottom row modulus images show a correlation between the phase quality and the signal modulus at a given area of the field of view. The phase is rather continuous in areas of high modulus, and on the other hand, when there is low signal modulus, there are phase jumps and ambiguities present.

For this reason, single images alone do not provide satisfactory representation of the examined specimen. However, as mentioned in Sec. 3.5, their complex image rep-

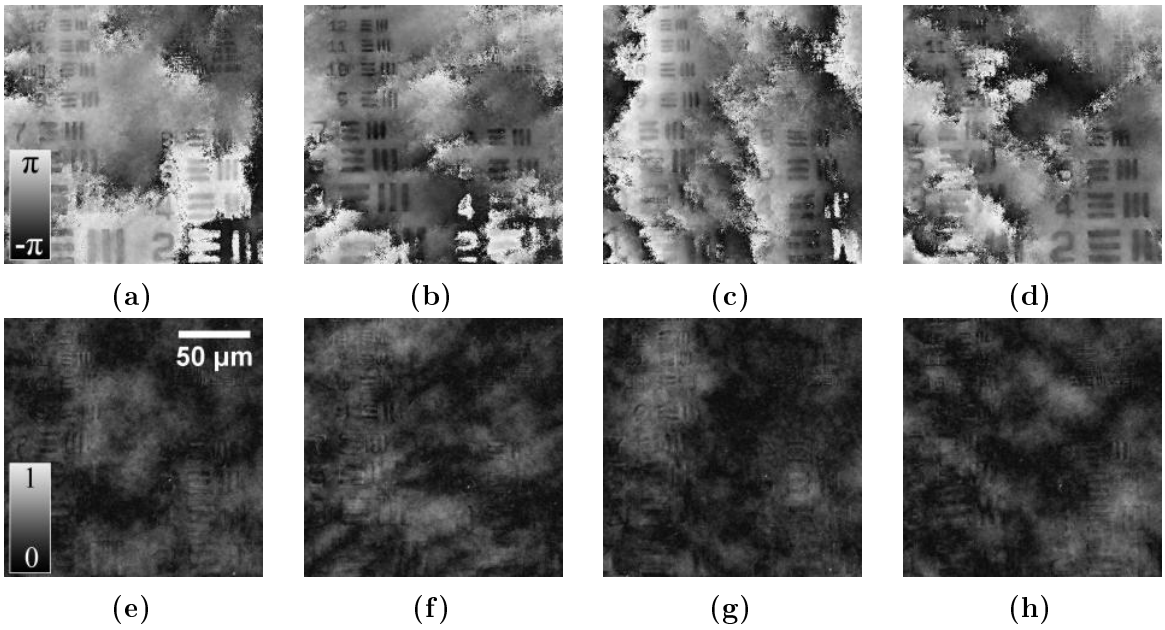

Figure 4.13: (a-d) Compensated phase images, their position in the acquired dataset is marked by blue color in Fig. 4.12. (e-h) Corresponding signal modulus images to (a-d), color indicates normalized modulus. Images are for the purpose of easier recognizability of resolution target rotated and flipped in relation to the original image.

resentations can be superposed and form more accurate image of the specimen.

Two synthetic images are presented in Fig. 4.14. They provide an insight into the image synthesis problem. They were created by the coherent summation of images acquired for different reference field shifts. In this process, areas with discontinuous phase have lower weight (because of lower signal modulus), and therefore, contribute to the final image minimally. However small is the modulus at these areas, summation of a large number of low quality images may corrupt the final image. As shown in Fig. 4.14b superposition of the whole image set, besides the ballistic image, creates an image with visible structures of the resolution target. Also the quantitative phase information is present, but its quality is reduced compared to the reference image in Fig. 4.1a. Another example of the synthetic image is in Fig. 4.14a, which is created out of a randomly chosen subset (40 images) of scattered light images. The comparison of these two synthetic images shows that better results are not necessarily obtained, if a large number of images is superposed. Some areas of the field of view are corrupted by the summation of more images then necessary, but some areas experience an improved phase quality and continuity.

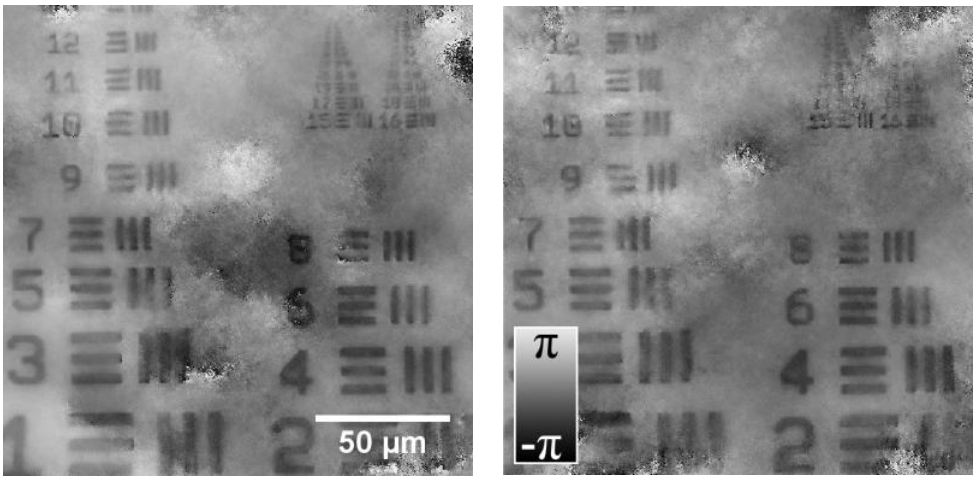

(a) **(b)**

Figure 4.14: (a) The synthetic quantitative phase image created by the sum of all images (acquired according to scheme in Fig. 3.10) besides the ballistic one (zero field shift). The image (b) is created by the sum of 40 randomly chosen images obtained just from the multiply scattered light. Images are for the purpose of easier recognizability of resolution target rotated and flipped in relation to the original image. ($NA_S = 0.30$, interference filter 650 nm/10 nm FWHM, objective lenses 20x/NA = 0.50)

4.4.2 Illumination by microscope objectives

Another experiment with the etched glass plate, but with a slightly different setting, was carried out. Numerical aperture of the illumination was extended to $\mathrm{NA_S} = 0.50$. Such an increase of $\mathrm{NA_S}$ was made possible by the exchange of the condenser lenses for microscope objectives (20x/NA = 0.50). This made the peak of the $s_\mathrm{t}(\mathbf{q}_\mathrm{t})$ function narrower, therefore, the separation of the scattered light is in this case more robust and the imaging gets closer to the ideal case described by (3.41). The relative positioning of the resolution target and the etched glass plate was not the same as in the experiment described in Subsec. 4.4.1, which means that the scattering strength was of the same order, but it resulted in a locally different scattering over the field of view.

The data set acquired in this experiment is shown in Fig. 4.15. This figure proves improved coherence-gate induced separation of the scattered light, because even images obtained for 1 µm field shifts start to experience linear phase distortion. This dataset is presented, because it shows the reason of the image synthesis. The experimental data presented before (the ground coverslip, and another setting with the etched glass plate) had both relatively undistorted ballistic light images. However, the ballistic light image (Fig. 4.18b) of the dataset presented in this subsection is corrupted and some regions of the field of view have low signal modulus, which also results in the low quality of the phase. The synthetic image is meant to provide a better phase image of the specimen than the distorted ballistic one.

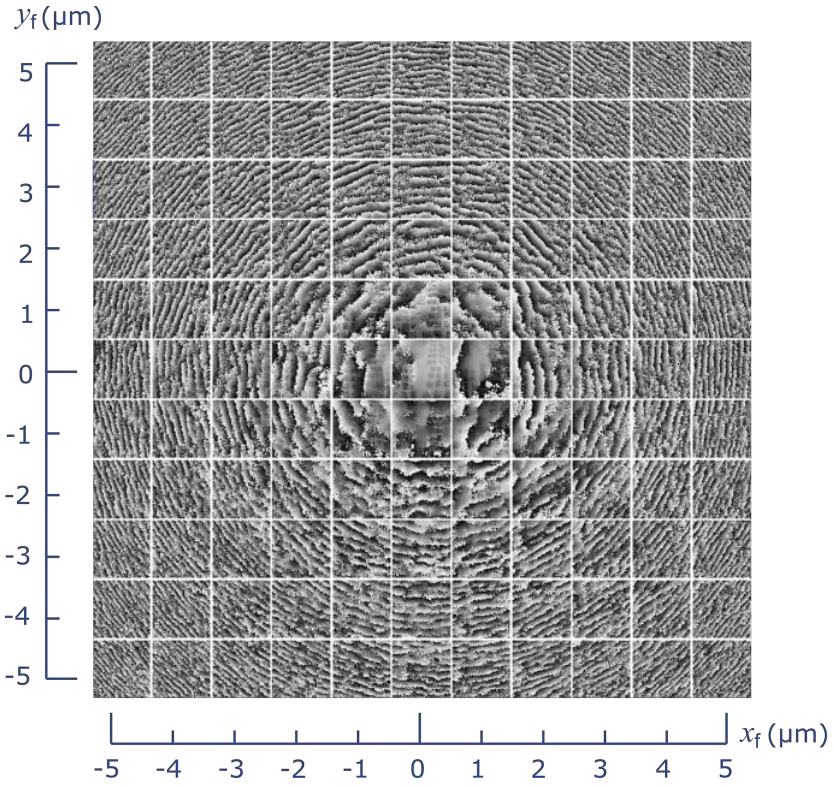

Figure 4.15: Composed image out of 121 non-compensated phase images obtained by scanning the objective lens in the reference arm according to the procedure described in Sec. 3.6 for the etched glass plate experiment with $\mathrm{NA_S} = 0.50$.

Average signal modulus of acquired images is similar to those in the previous experiment with etched glass plate. This is shown in Fig. 4.16. The central image modulus is of the same order as the modulus of scattered light images.

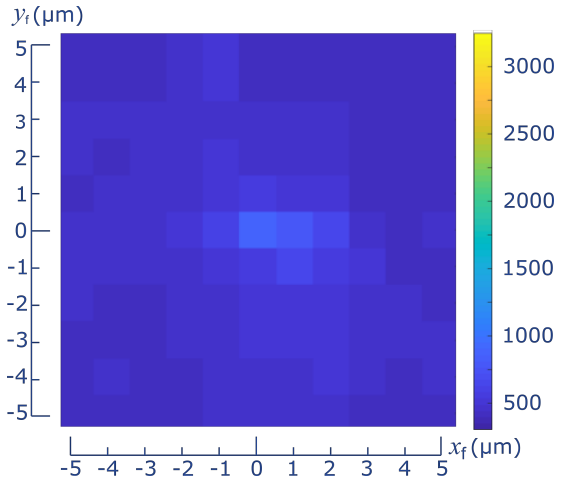

Figure 4.16: Average signal modulus map of acquired images for various shifts with resolution target and the etched glass plate as the diffuser ($NA_S = 0.50$). Color scale denotes the dimensionless modulus of the complex amplitude.

The compensation procedure was again carried out on all images of the dataset in Fig. 4.15. By looking at Fig. 4.17, it seems that the phase correction was successful for all the images, because there is not any obvious phase ramp.

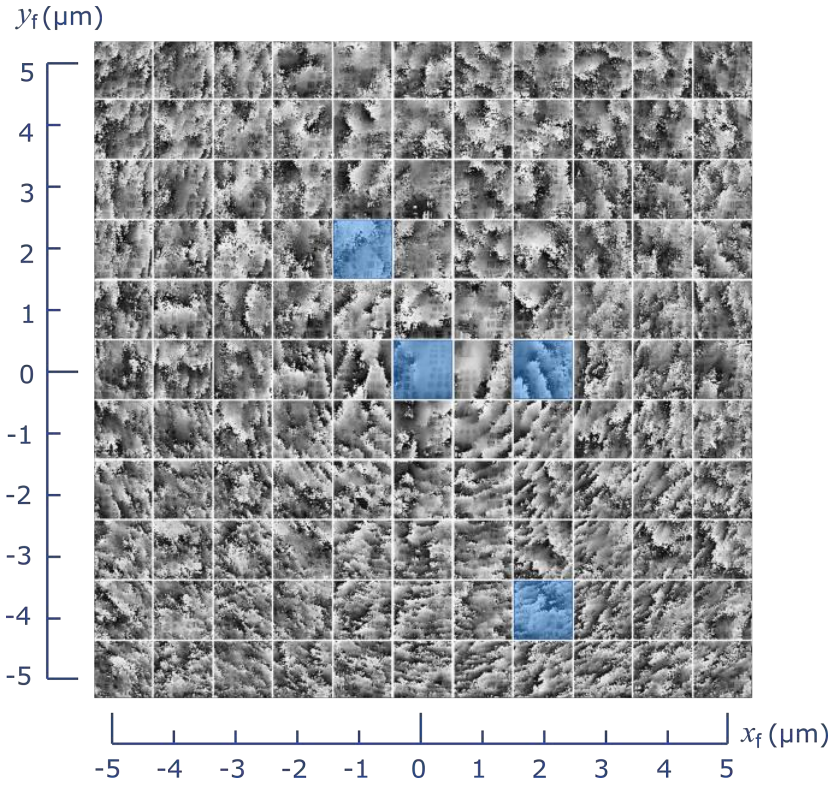

Figure 4.17: Composed image of compensated phase images of the dataset for the etched glass plate diffuser and $NA_S = 0.50$. Phase compensation used is described in Sec. 3.4.

However, the outcome of the image synthesis is dependent on the optimization approach, which will be shown later in this subsection, and is hard to predict just by looking at the single compensated images. Four images (marked by the blue color in Fig. 4.17) in Fig. 4.18 are showing again the strong relation between the signal modulus of the field of view area and the phase quality in that region.

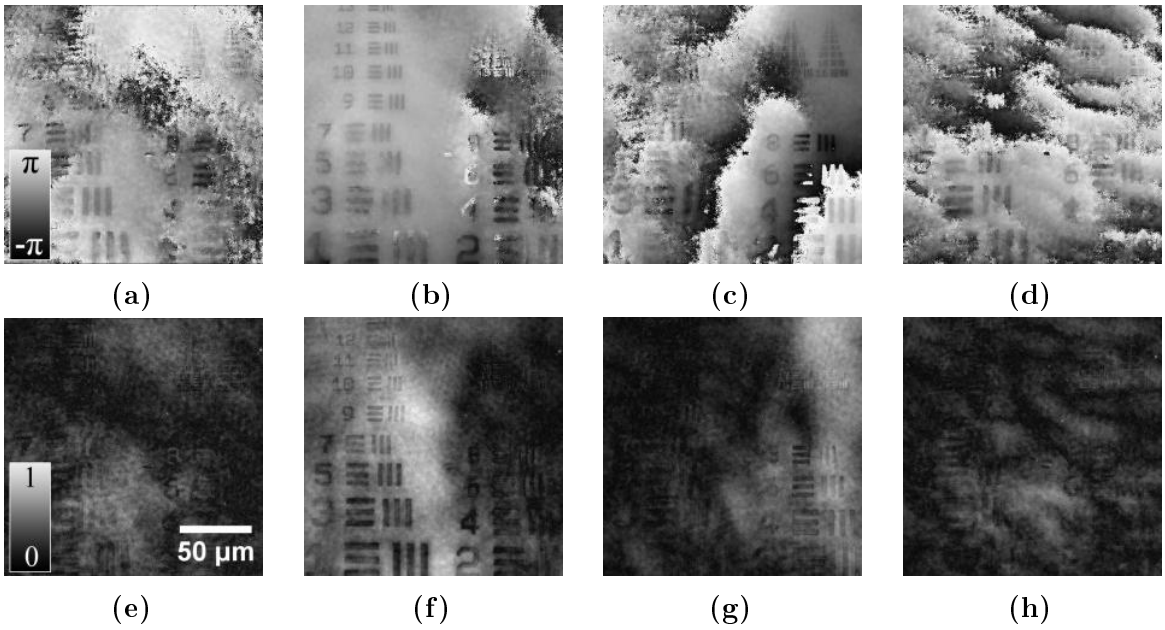

Figure 4.18: (a-d) Compensated phase images, their position in the acquired dataset is marked by blue color in Fig. 4.17. (e-h) Corresponding signal modulus images to (a-d), color indicates normalized modulus. Images are for the purpose of easier recognizability of resolution target horizontally flipped in relation to the original image. ($NA_S = 0.50$, interference filter 650 nm/10 nm FWHM, objective lenses 20x/NA = 0.50)

Two synthesized images were created out of this dataset. The first one (Fig. 4.20a) is created by a superposition of all images, besides the ballistic one, while the optimization procedure was done according to Subsec. 3.4.2, where the average signal modulus is calculated from the whole field of view. The synthetic image (Fig. 4.20a) provides little improvement in the area, where the ballistic one (Fig. 4.18b) is corrupted. This is caused by an optimization procedure setting. The iterative process in a case, in which the ballistic image modulus experiences high values in some areas and *significantly* lower values in other areas of the field of view, inherently optimizes the phase continuity in those regions of higher modulus. Therefore, the synthetic reconstruction may not provide the lost (due to scattering) information.

The second synthesized image (Fig. 4.20b) is created out of images, which were optimized by a modified iterative approach. The average modulus in (3.43) is in this case calculated over a defined region of the ballistic light image, the region of confinement of the $\mathbf{q}_t$ is shown in Fig. 4.19. The synthetic image in Fig. 4.20b shows that the phase is continuous in the region of interest, but on the other hand, other areas suffer from phase distortions and ambiguities.

Figure 4.19: Ballistic light phase image where the blue colored region is subject of the optimization procedure. Acquired by CCHM ($NA_S = 0.50$, interference filter 650 nm/10 nm FWHM, objective lenses 20x/NA = 0.50).

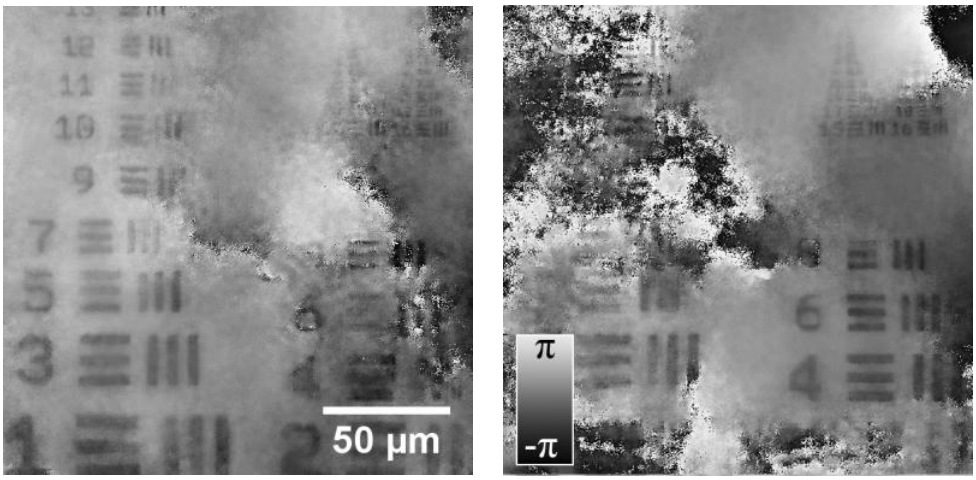

(a) **(b)**

Figure 4.20: (a) Superposition of all images besides the ballistic one for optimization of the whole field of view, (b) Superposition of all images besides the ballistic one for optimization focused on a low quality region of the ballistic image. Images are for the purpose of easier recognizability of resolution target flipped in relation to the original image. ($NA_S = 0.50$, interference filter 650 nm/10 nm FWHM, objective lenses 20x/NA = 0.50)

4.5 Volume diffuser

Previous experiments involved planar diffusers. However, in biological tissues the scattering at one plane of the sample occurs very rarely. Therefore, a volume scattering media have to be examined. For this purpose an experiment with milk mixture as the diffusive medium was carried out. A whole milk (3.5 % of fat) was mixed with a distilled water to adjust the concentration. Mixtures of various ratios were prepared and the resolution target was observed through each of them. The diluted milk was inserted into a channel slide (ibidi µ-Slide I Luer 0.8 mm thick), and as shown in Fig. 4.1b, joined with the resolution target and the coverslip to form an object that was placed into the object arm of CCHM.

In this section, an experiment with the milk to distilled water ratio of 1:2 is presented. A slightly different transverse shifts of the reference field were used, as can be seen from the composed image in Fig. 4.21. The average signal modulus shown in Fig. 4.22 provides information about scattering properties of the mixture. The signal modulus in central images is similar to the one of ballistic image in Fig. 4.16, however, for greater transverse shifts, the signal modulus is lower than in the experiment with the etched glass plate or the ground coverslip. This means, the absorption of light is higher in the milk, and the scattering is weaker than in the previous experiments. It may be also accounted to the increased thickness of the diffusive medium. Scattered

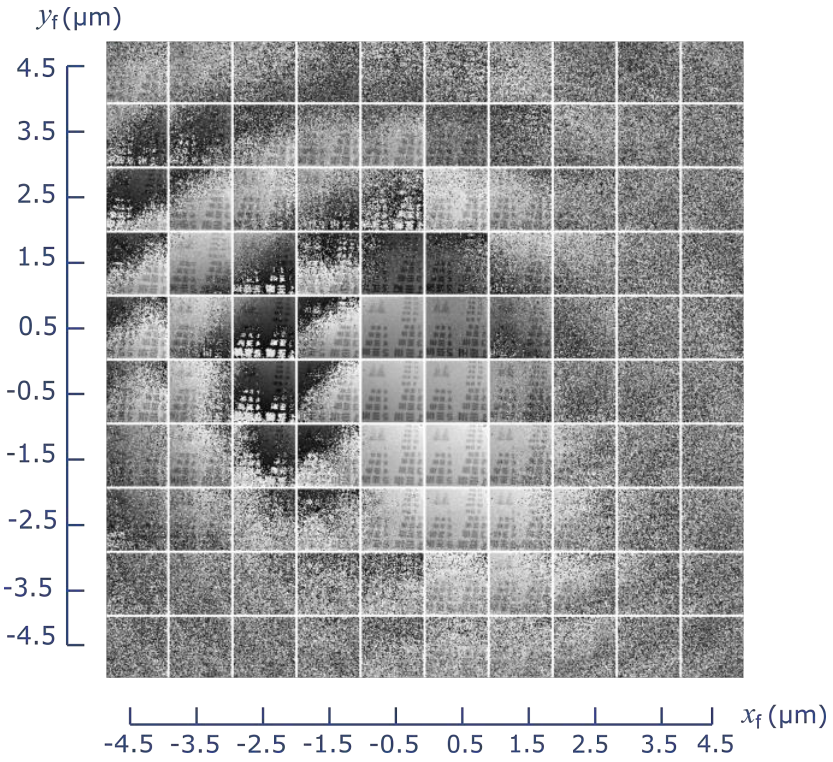

Figure 4.21: Composed image of phase images of the dataset acquired through a milk mixture. ($NA_S = 0.30$, interference filter 650 nm/10 nm FWHM, objective lenses 20x/NA = 0.50)

light images (Fig. 4.21) do not show in this case of a volume diffuser any pronounced linear phase modulation, but according to (3.41), the phase modulation is present. Be-

cause the scattering is not happening only in one plane of defined distance z_D from the specimen, the phase distortion cannot be predicted, and therefore, it is hard to compensate.

There were though some attempts to synthesize an image out of this dataset. A phase compensation, which was based on the one mentioned in Sec. 3.4, could not provide any viable results. Also coherent summation had not resulted in an image with resolvable structure of the phase test target. As expected, the proposed method of image synthesis out of scattered light images does not work in this case, and the imaging can be for now provided only by the separation of ballistic light from the diffuse light by the coherence gate.

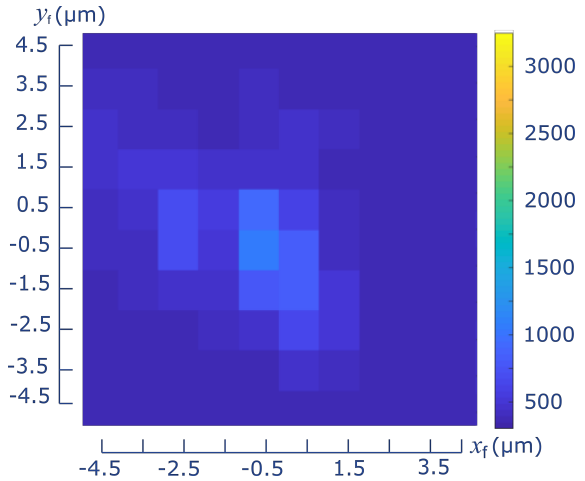

Figure 4.22: Average signal modulus map of acquired images for various shifts with resolution target and the milk mixture as the diffuser. Color scale denotes the dimensionless modulus of the complex amplitude.

5. Discussion

Experimental results, which are presented in Chap. 4, provided a confirmation of theoretically predicted strong coherence-gating capabilities of CCHM. The coherence gate of CCHM allows to image in highly disordered scattering media, which are seemingly opaque. It increases the number of possible CCHM applications. Experiments show that the separation of a ballistic light, when it is relatively dominant over a diffuse light, is sufficiently strong. However, the coherence gate (provided by the low spatial coherence of the illumination) filters out only spatially deviated photons. If only the spatial filtering is applied, quantitative phase image may still be distorted. Photons, which are not spatially deviated, but only time-delayed, are not filtered by spatial filtering effect of the coherence gate. These photons contribute to the image modulus of the specimen positively, but QPI is negatively distorted by them. These photons can be separated in a similar manner as the spatially deviated ones by a broadband source, which decrease the temporal coherence of the light and makes the time-gating possible. For example image in Fig. 4.3a is minimally distorted by the spatially deviated photons, which are filtered out thanks to the spatially broad source. However, some distortions and noise is present. This is caused by the time-delayed photons, which are allowed to interfere, because an interference filter with central wavelength of 650 nm and FWHM of 10 nm is used. With these parameters, the estimated coherence length, according to a formula derived in [57], is about 28 µm. This is a relatively long coherence length in comparison to the depth of the etched or ground features of diffusers. Further experiments with broader wavelength spectrum have to be carried out to analyze an impact of increased time-gating effect on QPI. A reduced noise levels and fewer phase distortions are expected.

Weak diffusers, like the one examined in Sec. 4.3, are characterized by a high ballistic light transmission. Despite the fact that scattered light signal modulus is almost an order lower than the ballistic light component, it can still severely degrade QPI in coherent illumination. The diffuse light of low modulus cannot be sufficiently separated from the ballistic light, which experiences a strong peak. The high signal modulus of the ballistic light, which is accompanied with a low standard deviation of phase values (see Sec. 3.5), and the inability to completely separate the least-scattered from the multiply scattered light indicates that the best way to image through weakly scattering media in CCHM is to use only the single (central) ballistic light image. This is supported by the result in Fig. 4.8a.

When a sample is strongly scattering, and the ballistic image is no longer providing a reliable information about the observed part of the sample, then synthetic image may provide an alternative way to examine a specimen. Experimental results shown in Sec. 4.4, prove the concept of image synthesis, however, they also show some drawbacks of the proposed synthesis method. The scattered light is sufficiently separated and the

phase distortion can be partially compensated. The compensated phase images have to be treated by an additional optimization procedure, which affects the outcome of the image synthesis. Fig. 4.20a proves the synthetic image has slightly better quality than the ballistic image, and image in Fig. 4.20b, created by a region optimization, proves that the information, which is not in the ballistic light image, is scattered and can be retrieved from images formed by the scattered light only. In many cases, a routine acquisition of a predefined dataset and a phase compensation described in Sec. 3.4 followed by a superposition of compensated images create a synthetic image of improved quality in comparison to the ballistic image. However, there is still room for an improvement in terms of a better phase compensation and selection of images, which are used for the synthesis. There are already emerging new ideas, which may further improve the image synthesis. For example, a feedback loop could be implemented in the image acquisition process, which would provide information to the system about the signal modulus value at a current reference arm objective position.

An outcome of experiments involving volume diffusers can be predicted by (3.41). Each scattering layer positioned at different distance z_{D} from a specimen produces also different phase modulation of the image of the specimen. If this phase modulation could be removed, the image of the specimen could be retrieved and used for the image synthesis. The phase compensation of images obtained through volume diffusers represents a challenging problem, which requires a further investigation.

6. Conclusion

The thesis deals with the use of the coherence-gating property of coherence-controlled holographic microscope in the imaging of objects in turbid milieu. Goals of this thesis are interconnected with the previous research performed by Experimental Biophotonics group in the field of low-coherence digital holography, quantitative phase imaging and coherence-gated turbid media imaging. The main aim of the work is to deepen the knowledge about QPI through scattering media by a theoretical and an experimental investigation. Preliminary research suggests that a combination of ballistic and multiply scattered photons may improve the quality of QPI. The first goal is to design a method, which would provide a routine observation technique in strongly scattering media. An experimental verification of the designed method on a suitable sample is the second goal of the thesis.

In this thesis, a completely novel method of synthetic image creation is proposed. It is mainly based on the analytical derivations. Experimental data verified the image synthesis applicability in QPI and also provided an information needed for the optimization of the proposed method. The image synthesis procedure consist of several steps: the image acquisition of a set of images formed by the multiply scattered light, the phase compensation of acquired images and the synthesis of the final image by the coherent superposition of phase compensated images.

Therefore, it can be concluded that the goals of thesis have been achieved and the author of this thesis contributed to the research field of QPI in turbid media in numerous ways:

- A simplified approximative solution of the image formation through scattering layers in CCHM has been derived, see Subsec. 3.3.3. It provides a good starting point in the explanation of an impact of a scattering process on a reconstructed holographic image.

- Based on the knowledge provided by the preliminary research [22,24,41] an image synthesis method was designed (Sec. 3.5, Sec. 3.6). It exploits the coherence-gating properties of CCHM to separate ballistic and multiply scattered light and uses numerous images formed by scattered photons to create a synthetic image of improved quality. Results are presented in Sec. 4.4 in Fig. 4.14 and Fig. 4.20.

- Experiments had shown that in order to successfully synthesize an image a phase compensation step is required. Therefore, methods of phase compensation (Sec. 3.4) have been proposed and applied successfully to the experimental data.

- Extensive experiments using various samples have been carried out (some of them are presented in Chap. 4). The outcomes of the experimental work have proved

many principles that are based on the analytical results and provided a valuable supportive knowledge.

- A novel routine observation method of specimen placed behind a strongly scattering layer has been designed. It is already partially implemented in the control software of CCHM.

Results of this work have been already presented at SPIE Photonics Europe conference and have been published in the proceeding paper [56].

Bibliography

[1] RUDOLPH, W. KEMPE, M.: Trends in optical biomedical imaging. *Journal of Modern Optics*, vol. 44, no. 9, 1997: pp. 1617–1642, ISSN 13623044, Available from: doi:10.1080/09500349708230763.

[2] DILWORTH, D. S., LEITH, E. N. LOPEZ, J. L.: Imaging absorbing structures within thick diffusing media. *Applied optics*, vol. 29, no. 5, 1990: pp. 691–698, Available from: doi:10.1364/AO.29.000691.

[3] KEMPE, M., RUDOLPH, W. WELSCH, E.: Comparative study of confocal and heterodyne microscopy for imaging through scattering media. *Journal of the Optical Society of America A*, vol. 13, no. 1, 1996: p. 46, ISSN 1084-7529, Available from: doi:10.1364/JOSAA.13.000046.

[4] KEMPE, M. et al.: Ballistic and diffuse light detection in confocal and heterodyne imaging systems. *J. Opt. Soc. Am. A*, vol. 14, no. 1, 1997: pp. 216–223, ISSN 1084-7529, Available from: doi:10.1364/JOSAA.14.000216.

[5] WANG, L. M., HO, P. P. ALFANO, R. R.: Double-stage picosecond Kerr gate for ballistic time-gated optical imaging in turbid media. *Applied optics*, vol. 32, no. 4, 1993: pp. 535–540, ISSN 0003-6935, Available from: doi:10.1364/AO.32.000535.

[6] HEBDEN, J. C. KRUGER, R. A.: Transillumination imaging performance: A time-of-flight imaging system. *Medical Physics*, vol. 17, no. 3, 1990: pp. 351–356, Available from: doi:10.1118/1.596514.

[7] CAULFIELD, H. J.: Holographic Imaging Through Scatterers. *Journal of the Optical Society of America*, vol. 58, no. 2, 1968: pp. 276–277, ISSN 0030-3941, Available from: doi:10.1364/JOSA.58.000276.

[8] LEITH, E. N. KUEI, C. P.: Interferometric method for imaging through inhomogeneities. *Optics letters*, vol. 12, no. 3, 1987: pp. 149–51, ISSN 0146-9592, Available from: doi:10.1364/OL.12.000149.

[9] LEITH, E. N. et al.: Imaging through scattering media using spatial incoherence techniques. *Optics Letters*, vol. 16, no. 23, 1991: p. 1820, ISSN 0146-9592, Available from: doi:10.1364/OL.16.001820.

[10] LEITH, E. et al.: Imaging through scattering media with holography. *Journal of the Optical Society of America A*, vol. 9, no. 7, 1992: pp. 1148–1153, ISSN 1084-7529, Available from: doi:10.1364/JOSAA.9.001148.

[11] SLABÝ, T. et al.: Off-axis setup taking full advantage of incoherent illumination in coherence-controlled holographic microscope. *Optics Express*, vol. 21, no. 12, 2013: pp. 14747–62, ISSN 1094-4087, Available from: doi:10.1364/OE.21.014747.

[12] CHMELIK, R. et al.: The Role of Coherence in Image Formation in Holographic Microscopy. *Progress in Optics*, vol. 59, 2014: pp. 267–335, ISSN 0079-6638, Available from: doi:10.1016/B978-0-444-63379-8.00005-2.

[13] DURDURAN, T. et al.: Diffuse Optics for Tissue Monitoring and Tomography. *Reports on progress in physics. Physical Society (Great Britain)*, vol. 73, no. 7, 2010, ISSN 1361-6633, Available from: doi:10.1088/0034-4885/73/7/076701.

[14] VAN ROSSUM, M. C. W. NIEUWENHUIZEN, T. M.: Multiple scattering of classical waves: microscopy, mesoscopy, and diffusion. *Reviews of Modern Physics*, vol. 71, no. 1, 1999: pp. 313–371, ISSN 0034-6861, Available from: doi:10.1103/RevModPhys.71.313.

[15] POPPOF, S. et al.: Controlling Light Through Optical Disordered Media : Transmission Matrix Approach. *New Journal of Physics*, vol. 13, no. 12, 2011: p. 123021.

[16] YAQOOB, Z. et al.: Optical phase conjugation for turbidity suppression in biological samples. *Nature Photonics*, vol. 2, no. 2, 2008: pp. 110–115, ISSN 17494885, Available from: doi:10.1038/nphoton.2007.297.

[17] CHOI, Y. et al.: Optical imaging with the use of a scattering lens. *IEEE Journal on Selected Topics in Quantum Electronics*, vol. 20, no. 2, 2014: pp. 61–73, ISSN 1077260X, Available from: doi:10.1109/JSTQE.2013.2275942.

[18] ĎURIŠ, M. et al.: Towards an ultra-thin medical endoscope: multimode fibre as a wide-field image transferring medium. In *2nd Canterbury Conference on OCT with Emphasis on Broadband Optical Sources*, vol. 10591, ed. by O. Bang; A. Podoleanu, SPIE, 2018, ISBN 9781510616745, p. 34, Available from: doi:10.1117/12.2283482.

[19] EDREI, E. SCARCELLI, G.: Memory-effect based deconvolution microscopy for super-resolution imaging through scattering media. *Scientific Reports*, vol. 6, no. April, 2016: pp. 1–8, ISSN 20452322, Available from: doi:10.1038/srep33558.

[20] FREUND, I., ROSENBLUH, M. FENG, S.: Memory effects in propagation of optical waves through disordered media. *Physical Review Letters*, vol. 61, no. 20, 1988: pp. 2328–2331, ISSN 00319007, Available from: doi:10.1103/PhysRevLett.61.2328.

[21] LEITH, E. N. UPATNIEKS, J.: Holography with Achromatic-Fringe Systems*. *Journal of the Optical Society of America*, vol. 57, no. 8, 1967: p. 975, ISSN 0030-3941, Available from: doi:10.1364/JOSA.57.000975.

[22] LOŠT'ÁK, M. et al.: Coherence-controlled holographic microscopy in diffuse media. *Optics Express*, vol. 22, no. 4, 2014: p. 4180, ISSN 1094-4087, Available from: doi:10.1364/OE.22.004180.

[23] COLLAKOVA, J. et al.: Coherence-controlled holographic microscopy enabled recognition of necrosis as the mechanism of cancer cells death after exposure to cytopathic turbid emulsion. *Journal of Biomedical Optics*, vol. 20, no. 11, 2015: p. 111213, ISSN 1083-3668, Available from: doi:10.1117/1.JBO.20.11.111213.

[24] KOLLAROVA, V. et al.: Quantitative phase imaging through scattering media by means of coherence-controlled holographic microscope. *Journal of Biomedical Optics*, vol. 20, no. 11, 2015: p. 111206, ISSN 1083-3668, Available from: doi:10.1117/1.JBO.20.11.111206.

[25] BOHREN, C. F. HUFFMAN, D. R.: *Absorption and Scattering of Light by Small Particles*. Weinheim, Germany: Wiley-VCH Verlag GmbH, 1998, ISBN 9783527618156, 530 pp., Available from: doi:10.1002/9783527618156.

[26] LELLI, L.: Aerosol and Clouds WS2014 - Scattering Regimes. 2014. URL <http://www.iup.uni-bremen.de/~luca/?download=01_LL_V0.pdf>

[27] FARAGE, M. A. et al.: Structural Characteristics of the Aging Skin: A Review. *Cutaneous and Ocular Toxicology*, vol. 26, no. 4, 2007: pp. 343–357, ISSN 1556-9527, Available from: doi:10.1080/15569520701622951.

[28] TUCHIN, V. V.: *Tissue Optics: Light Scattering Methods and Instruments for Medical Diagnosis*. SPIE, 2015, ISBN 9781628415162, 988 pp., Available from: doi:10.1117/3.1003040.

[29] ROGERS, J. D. et al.: Modeling Light Scattering in Tissue as Continuous Random Media Using a Versatile Refractive Index Correlation Function. *IEEE journal of selected topics in quantum electronics : a publication of the IEEE Lasers and Electro-optics Society*, vol. 20, no. 2, 2013: p. 7000514, ISSN 1077-260X, Available from: doi:10.1109/JSTQE.2013.2280999.

[30] XU, M.: Plum pudding random medium model of biological tissue toward remote microscopy from spectroscopic light scattering. *BIOMEDICAL OPTICS EXPRESS*, vol. 8, no. 6, 2017: pp. 2879–2895, ISSN 21567085, Available from: doi:10.1364/BOE.8.002879, <1709.00795>.

[31] SI, K., GONG, W. SHEPPARD, C. J. R.: Model for light scattering in biological tissue and cells based on random rough nonspherical particles. *Applied Optics*, vol. 48, no. 6, 2009: p. 1153, ISSN 0003-6935, Available from: doi:10.1364/AO.48.001153.

[32] SHEPPARD, C. J. R.: Fractal model of light scattering in biological tissue and cells. *Optics Letters*, vol. 32, no. 2, 2007: p. 142, ISSN 0146-9592, Available from: doi:10.1364/OL.32.000142.

[33] XIE, S., LI, H. LIN, L.: Light scattering model for biological tissue. In *Laser-Tissue Interaction XI: Photochemical, Photothermal, and Photomechanical*, vol. 3914, 2000, pp. 522–526.

[34] SCHMITT, J. M. KUMAR, G.: Turbulent nature of refractive-index variations in biological tissue. *Optics letters*, vol. 21, no. 16, 1996: pp. 1310–2, ISSN 0146-9592, Available from: doi:10.1364/OL.21.001310.

[35] ISHIMARU, A.: *Wave propagation and scattering in random media*. IEEE Press, 1997, ISBN 9780780347175, 574 pp.

[36] BORN, M. WOLF, E.: *Principles of optics : electromagnetic theory of propagation, interference and diffraction of light*. Cambridge University Press, 1999, ISBN 9781139644181, 952 pp.

[37] TUCHIN, V.: Tissue Optics and Photonics: Light-Tissue Interaction II. *Journal of Biomedical Photonics & Engineering*, vol. 2, no. 3, 2016: p. 030201, ISSN 24112844, Available from: doi:10.18287/JBPE16.02.030201.

[38] BARBER, P. W. WANG, D.-S.: Rayleigh-Gans-Debye applicability to scattering by nonspherical particles. *Applied Optics*, vol. 17, no. 5, 1978: p. 797, ISSN 0003-6935, Available from: doi:10.1364/AO.17.000797.

[39] TOUBLANC, D.: Henyey–Greenstein and Mie phase functions in Monte Carlo radiative transfer computations. *Applied Optics*, vol. 35, no. 18, 1996: p. 3270, ISSN 0003-6935, Available from: doi:10.1364/AO.35.003270.

[40] HENYEY, L. C. GREENSTEIN, J. L.: Diffuse radiation in the Galaxy. *The Astrophysical Journal*, vol. 93, 1941: p. 70, ISSN 0004-637X, Available from: doi:10.1086/144246.

[41] HENZLOVÁ, M., LOŠŤÁK, M. CHMELÍK, R.: Theoretical study of coherence-controlled holographic microscopy in the presence of scattering media. *Proc.SPIE*, vol. 8697, 2012: p. 869713, Available from: doi:10.1117/12.2012361.

[42] BASKIN, R. J., ROOS, K. P. YEH, Y.: Light diffraction study of single skeletal muscle fibres. *Biophysical journal*, vol. 28, no. 1, 1979: pp. 45–64, ISSN 0006-3495, Available from: doi:10.1016/S0006-3495(79)85158-9.

[43] ZERNIKE, F.: How I discovered phase contrast. *Science (New York, N.Y.)*, vol. 121, no. 3141, 1955: pp. 345–9, ISSN 0036-8075, Available from: doi:10.1126/SCIENCE.121.3141.345.

[44] BARER, R.: Interference Microscopy and Mass Determination. *Nature*, vol. 169, no. 4296, 1952: pp. 366–367, ISSN 0028-0836, Available from: doi:10.1038/169366b0.

[45] ZANGLE, T. A. TEITELL, M. A.: Live-cell mass profiling: An emerging approach in quantitative biophysics. *Nature Methods*, vol. 11, no. 12, 2014: pp. 1221–1228, ISSN 15487105, Available from: doi:10.1038/nmeth.3175, <NIHMS150003>.

[46] KASTL, L. et al.: Quantitative phase imaging for cell culture quality control. *Cytometry Part A*, vol. 91, no. 5, 2017: pp. 470–481, ISSN 15524930, Available from: doi:10.1002/cyto.a.23082.

[47] CREATH, K.: V Phase-Measurement Interferometry Techniques. *Progress in Optics*, vol. 26, 1988: pp. 349–393, ISSN 0079-6638, Available from: doi:10.1016/S0079-6638(08)70178-1.

[48] KREIS, T.: Digital holographic interference-phase measurement using the Fourier-transform method. *Journal of the Optical Society of America A*, vol. 3, no. 6, 1986: p. 847, ISSN 1084-7529, Available from: doi:10.1364/JOSAA.3.000847.

[49] HEWITT, E. HEWITT, R. E.: The Gibbs-Wilbraham phenomenon: An episode in fourier analysis. *Archive for History of Exact Sciences*, vol. 21, no. 2, 1979: pp. 129–160, ISSN 0003-9519, Available from: doi:10.1007/BF00330404.

[50] WOLF, E.: Electromagnetic Diffraction in Optical Systems. I. An Integral Representation of the Image Field. *Proceedings of the Royal Society A: Mathematical, Physical and Engineering Sciences*, vol. 253, no. 1274, 1959: pp. 349–357, ISSN 1364-5021, Available from: doi:10.1098/rspa.1959.0199.

[51] WOLF, E.: Three-dimensional structure determination of semi-transparent objects from holographic data. *Optics Communications*, vol. 1, no. 4, 1969: pp. 153–156, ISSN 0030-4018, Available from: doi:10.1016/0030-4018(69)90052-2.

[52] MANDEL, L. WOLF, E.: Coherence properties of optical fields. *Reviews of Modern Physics*, vol. 37, no. 2, 1965: pp. 231–287, ISSN 00346861, Available from: doi:10.1103/RevModPhys.37.231.

[53] WEISSTEIN, E. W.: Delta Function From MathWorld—A Wolfram Web Resource. *Wolfram Research, Inc.* 2004, [online] [cit. 2018-05-08]. URL <http://mathworld.wolfram.com/DeltaFunction.html>

[54] RUDER, S.: An overview of gradient descent optimization algorithms. *Cornell University Library*, vol. abs/1609.0, 2016, <1609.04747>.

[55] CHMELÍK, R.: *Korelační mikroskopie, alternativní metoda vícekanálového konfokálního zobrazení.* Habilitation thesis, Brno University of Technology, 2001.

[56] CHMELÍK, R., DURIS, M. ŠTRBKOVÁ, L.: Quantitative phase imaging in turbid media by coherence controlled holographic microscopy. *Proc.SPIE*, vol. 10677, 2018: pp. 10677 – 10677 – 11, Available from: doi:10.1117/12.2309907.

[57] AKCAY, C., PARREIN, P. ROLLAND, J. P.: Estimation of longitudinal resolution in optical coherence tomography. *Applied Optics*, vol. 41, no. 25, 2002: pp. 5256–5262.